Received: 9 July 2019 | Revised: 8 November 2019 | Accepted: 21 January 2020

DOI: 10.1002/aic.16931

PARTICLE TECHNOLOGY AND FLUIDIZATION

AIChE JOURNAL

On the fast modeling of species transport in fluidized beds using recurrence computational fluid dynamics

Firas Dabbagh[1] | Stefan Pirker[2] | Simon Schneiderbauer[1,2]

[1]Christian-Doppler Laboratory for Multi-scale Modelling of Multiphase Processes, Johannes Kepler University, Altenbergerstr, Linz, Austria

[2]Department of Particulate Flow Modelling, Johannes Kepler University, Altenbergerstr, Linz, Austria

Correspondence
Christian-Doppler Laboratory for Multi-scale Modelling of Multiphase Processes, Johannes Kepler University, Altenbergerstr 69, Linz, Austria.
Email: firas.dabbagh@jku.at

Funding information
Christian Doppler Association; The Austrian Research Promotion Agency (FFG)

Abstract

Due to variety of scale dynamics evolved in gas–solid flows, most of its numerical description is limited to expensive short durations. This has made the slow processes therein, such as the chemical species conversion, to be out of an appropriate reach. In this work, an application of the transport-based recurrence computational fluid dynamics (CFD) has been introduced for the fast modeling of passive scalar transport, which is considered as species conversion and heat transfer in fluidized beds. The methodology discloses the recurrent dynamics during a short-term full CFD simulation as Lagrangian shift operations upon which a passive scalar can infinitely be traced. Apart from convecting, a proper approach based on the turbulent kinetic energy of tracked dynamics is introduced for modeling the physical diffusion of the scalar transported. Our outcomes have revealed a subtle chasing to the full CFD species simulation with a speed-up up to 1,600.

KEYWORDS

fluidized bed, passive transport, recurrence CFD, two-fluid model (TFM)

1 | INTRODUCTION

"The arrival time of a space probe traveling to Saturn can be predicted more accurately than the behavior of a fluidized bed chemical reactor!".[1] Fluidized beds are systems with a bed of granular particles initially resting on a perforated bottom plate. When the inlet fluid is passed upward through the bottom plate, it suspends, or fluidizes, the particles to allow a liquid-like behavior of solids with a high effective contacting process. This contributes to the chief advantage of fluidized beds in providing a rigorous mixing and favorable heat and mass transfer characteristics. With these attributes, fluidized beds have occupied a high-ranking beneficial position in the chemical processing applications, such as the well-known fluidized catalytic cracking of petroleum oil, granulation for powder production, coal carbonization and gasification, coking, coating preparations, and also in nuclear fuel fabrication. However, fluidized beds reactors are challenging to design and scale-up. The dynamics involved composes into complex physical phenomena because of the multiscale nonlinear interactions between the solid and fluid phases. Therewith, the evolution of structures, on the other hand, is strongly dependent on the particle properties such as size, shape, and density.[2] This nature has engrossed Geldart[1] and many other scientists[3-5] in order to understand and predict accurately all involved dynamics of fluidized beds. Principally, the fluid flow interacts with the solid particles by the interstitial fluid drag. The particles among themselves induce kinetic, collisional, and frictional stresses and undergo to complicated deformations and influences of pressure gradient, rolling, and gravity forces. The heat is transferred within each single phase and also between them. These (spatial and temporal) small-scale (microscopic) interactions compose to larger (mesoscopic and macroscopic) interactions which take place between clusters of solid (emulsion) and fluid bubbles. The temporal evolution of the (microscopic) particle's collision dynamics lasts about few milliseconds, much shorter than the bubble evolution. While the bubbles in turn, move faster than the fluid slugs in the bed and phenomena as

heat transfer and chemical species conversions can take minutes or hours.

Nowadays, computational methods based on fundamental principles for resolving each particle–particle and fluid–particle interactions have allowed to explore many details of the underlying dynamics[6] in fluidized beds. Using the computational fluid dynamics (CFD) techniques or lattice Boltzmann methods, the fluid hydrodynamics (obeying Navier–Stokes equations) is investigated on finer grids than the particles separations disclosing all forces exerted on the particles surface (drag), and deducing improved empirical correlations.[7,8] The solid side contacting forces of collisions are pictured as either an event-driven hard sphere model or a time step-driven soft sphere approach. With all relevant active forces on individual grain, each particle's trajectory is computed with the aid of Newton's second law, which is referred as the discrete element method (DEM) introduced by Cundall and Strack.[9] Coupling CFD-DEM has been the most appropriate numerical modeling for the simulation of fluidized beds; however, the huge inherent computational effort makes its application impractical for large particulate systems.[10] It is, therefore, common to investigate fluidized beds in large processing units using averaged equations of motion.[11] Namely, by averaging Navier–Stokes equations over several particle diameters while the particles may still be treated as discrete elements (unresolved CFD-DEM),[12] the computational cost can be reduced, but now the solid–fluid interactions are modeled using empirical closures. Another alternative method is considering the solid particles as a separate continuum, like the fluid phase, and the motion of particles is analogously averaged out, in the so referred two-fluid model (TFM).[13,14] Therein, the solid stresses arising from particle–particle collisions, the transitional dispersion of grains, and rotational speeds are deduced by adopting the kinetic theory of granular flow.[15] Since TFM allows for coarser grids without demanding to track individual particles, it ends to be more suitable for large systems than CFD-DEM; however, it is still forbidding for huge industrial-scale reactors.

With the considerable developments of numerical methods, the coarse-graining models have appeared to upscale both CFD-DEM and TFM to macroscopic sizes. For instance, the parcel-based DEM methods handle in tracking a parcel of several solid constituents which interact with modified material parameters.[16-18] Likewise, the coarse-grained TFM leads to simulate larger systems on much coarser grids,[19] but with the requirement of fundamental considering to the subgrid heterogeneities.[19-29] Even though, using these methods, the plant-size reactors may be simulated, but they are bounded by short-term investigations due to the huge computational power needed. The time scale simulation remains of small rates in order to capture mathematically all relevant dynamics of collisions; and therefore, the slow processes, which take hours in large fluidized beds, are still inaccessible. Seeking a remedy, some of us have introduced the idea of recurrence CFD (rCFD) for pseudoperiodic flows.[30-33] Namely, the continuous reappearing (recurrent) structures of such dynamics, for instance, the gas bubbles evolution in bubbling fluidized beds, is considered and analyzed on the base of a short-term full CFD simulation, that is, CFD-DEM or TFM. Using these data fields, the recurrence plots[34] are generated to predict a recurrence path upon which a passive scalar can be transported till infinity. This new methodology has been successfully applied for the fast passive transportation in multiphase flows[30] and heat transfer prediction in fluidized beds,[31,32] basing on CFD-DEM simulations. Therein, the advancing time-extrapolation procedure, by which the passive scalar is propagated on candidate recurrent patterns, is established using three proposed models. The flow-based category[30] where the recurrent flux fields have to be provided in order to resolve either a convection-diffusion equation (Eulerian model) or a stochastic differential equation for a fluid-parcel trajectory (Lagrangian model). In the third model named as the transport-based rCFD model,[32,33] the recurrent fields are shorten to only start-end positions information with no a posteriori need to resolve any equation. In this work, we focus on the test and application of the third rCFD model for the fast passive prediction of species and temperature (considered as a passive scalar) reconstructed transport in a lab-scale bubbling fluidized bed. The TFM is used to perform a short-term full CFD simulation, during which all database is collected and analyzed in terms of the recurrence properties and rCFD process. The main content, herein, implicates enhancements of the transport-based rCFD methodology in relevance to evaluating the proper physical diffusion approach for the passive scalar transported. Namely, after tracing the scalar, different diffusion approaches have been applied on the base of an approximate local diffusion and the global balance of the mass concentration scalar and enthalpy in the domain. The methodology is adapted for the reconstruction procedure of species and temperature path, separately, and the advancing time-extrapolation process for the case of a continuous coming-in inlet species on the gas phase. Doing so, the results have shown a successful consistency with the full CFD evolution by consuming very cheap and short runtime computations.

The rest of the paper is arranged as follows. First, the TFM and rCFD methodologies, particularly the transport-based method, are explained in Section 2 and Appendix. Then, details of the simulated fluidized bed with the results of species and heat transport rCFD modeling are presented and discussed in Section 3. Therein, the main feature is about finding the proper approach of the physical diffusion part in the transport-based rCFD methodology. On the other hand, the adapted algorithm of rCFD to transport the solid and gas temperatures as interacted two scalars is also outlined. Finally, relevant results are summarized and conclusions are given in Section 4.

2 | THEORY

2.1 | Two-fluid model

In the framework of gas–solid fluidization, the dynamics is handled on (large-scale) local mean variable within the (continuum) TFM approach. Its transport equations given in the Appendix describe the Eulerian framework of mass, $\rho_{s/g}\epsilon_{s/g}$ and momentum, $\rho_{s/g}\epsilon_{s/g}\boldsymbol{u}_{s/g}$ balances, precisely, derived on each phase (Equation A1 in Appendix). Therein, ϵ denote the volume fraction, while ρ and $\boldsymbol{u} = (u, v, w)$, are the

density and velocity fields, respectively, in correspondence to the subscript gas (g) or solid (s) phase. In some cases of a cold fluidization is accompanied with nonreactive chemical species conversions, the involved transport dynamics, for each jth specie mass fraction γ_j, is described in Eulerian framework, likewise (Equation A14 in the Appendix). The species, therein, are principally diffused obeying the dilute approximation of Fick's law, and roughly consider an identical constant value of the diffusion coefficient D_j, on the solid and gas phases. For another particular fluidization, when a participating heat transfer is implied, the temperature on the gas T_g and solid T_s phases follows, as well, an Eulerian frame which describes the enthalpy transport $h_{s/g} = c_p^{s/g} T_{s/g}$ (Equation A15 in the Appendix), assuming constant specific heats $c_p^{s/g}$. The key element, therein, is about measuring the interphase heat transfer coefficient denoting the Nusselt number, Nu, where the solid thermal conductivity κ_s is rigorously considered fixed and equivalent to the gas phase one κ_g.

2.2 | Recurrence CFD

In previous work,[30] the idea of rCFD had been introduced as an approach that helps to model the long-term processes in massively large systems, such as the chemical species conversions. Its application implies disclosing the recurrence properties of the system, which access the similarity between states and determine its periodicity parameters. Namely, on the base of a short-term full CFD simulation, the evolution in time t of active patterns at different probes in the domain is considered to decide the recurrence period τ_{rec}, which has to exceed several pseudoperiodic periods τ_{p-p} of the system. This last is identified by performing a spectral analysis of the signals (see an example in Figure 4d for the probes taken of the studied fluidized bed). And, hence, the recurrence period should span multiple periods of the corresponding lowest-lying peak frequency (f_{crit}) of the energy spectra, that is,

$$\tau_{rec} \gg \tau_{p-p} = \frac{1}{f_{crit}}. \tag{1}$$

The recurrence time step Δt_{rec} is estimated from the consideration that a given field φ is not changing too strongly from one time step to the next, inside τ_{rec}. Meaning that,

$$\Delta t_{rec} \ll \sqrt{\frac{\langle \varphi^2 \rangle}{\langle \dot{\varphi}^2 \rangle}}, \quad \text{where} \quad \dot{\varphi}(t) = \frac{|\varphi(t+\Delta t) - \varphi(t)|}{\Delta t}, \tag{2}$$

and $\langle \cdot \rangle$ denotes the temporal averaging operator. In order to quantify the similarity of flow patterns between states, for example, t and $t' = t + \Delta t_{rec}$, the recurrence norm is defined as,[30]

$$R^{(\varphi)}(t,t') = 1 - \frac{\int d^3r (\varphi(t) - \varphi(t'))^2}{\max_{t,t'} \int d^3r (\varphi(t) - \varphi(t'))^2}, \tag{3}$$

where φ can be chosen depending on the phenomenon of interest. And, by considering a series of stored fields the recurrence matrix can be obtained as

$$R_{n,m} \equiv R(n\Delta t_{rec}, m\Delta t_{rec}) \tag{4}$$

(see examples in Figures 5a,b, showing the recurrence matrix computed in respect of the solid volume fraction $R^{(\epsilon_s)}$ and solid flux $R^{(\epsilon_s \boldsymbol{u}_s)}$, respectively, for the studied fluidized bed).

Basing on the recurrence matrix, a recurrence path can be extracted to convey the system's evolution far beyond the recording time τ_{rec}. The strategy adopted was previously explained in,[30,31] and here we recall it in a simplified flow frames, f, aspect, shown in Figure 1. Namely, basing on $R(500, 500)$, and starting from the end f_{500}, we look for the most similar state by jumping backward toward the first half of τ_{rec}, and considering the original flow of the maximum R frame, that is, $f_{130} \approx f_{500}$. This frame will be taken as a base start field for the propagation of the passive scalar. Next, we pick an interval of random length $\Delta\tau > \Delta t_{rec}$ below the recurrence matrix size and construct the subsequent runtime of the frames, for example, f_{130}, f_{131}, f_{132},..., f_{200}. At the end of the interval, we jump again toward a similar state (maximized R) that better fits the end, that is, $f_{200} \approx f_{365}$. Depending on which half the end is, we pick the following state in the other such that R is maximized, and consider again another random interval. The process can continue till infinity and leads eventually to a discrete time series, that is, $\{f_{500} \approx f_{130}, f_{131}, f_{132}, ..., f_{200} \approx f_{365}, f_{366}, ..., f_{400} \approx f_{75}, f_{76}, ...\}$ that convects a passive process with a temporal lag Δt_{rec}.

In the so-called transport based rCFD model,[32,33] the online recurrent flow patterns evolving during τ_{rec} (for each Δt_{rec}), and which are needed to generate the flow candidature of the passive process, are considered in a Lagrangian sense. Namely, we describe the methodology as a tracer-based method that depends on tracking the dynamics, of the gas or solid phase or both, following inertia-less particles/tracers trajectories produced each Δt_{rec}. If these Lagrangian tracers are projected on the computational grid cells, the model ends to recurrent shift information stored in memory. Hence, in order to trace the propagation of the passive scalar, afterward, the model has only to shift the scalar information from the corresponding start to the receiving end cells, following the recurrent sequence control. In a practical inspection the methodology conducts the injection of internal massless tracers inside the domain with a seeding volume, $V_{tr} \le V_{cell}$, the volume of one cell, at the beginning of each Δt_{rec}. For the sake of an appropriate parameterization of the coming-in and going-out flow fluxes, another specific inlet and outlet tracers are accounted by different particular volumes. Namely, the inlet flux is approximated by setting a number of inlet tracers at the inlet surfaces of the domain, A_{in}, with discretization volumes equal to $V_{tr}^{inlet} = \epsilon_{s/g} ||\boldsymbol{u}_{in}|| A_{in} \Delta t_{rec}$ (see the corresponding subset of Step (1) in Figure 2). As graphically interpreted, this volume, V_{tr}^{inlet}, can be smaller or bigger than the neighboring-cell volume V_{bc}. In case of $V_{tr}^{inlet} = \epsilon_{s/g} ||\boldsymbol{u}_{in}|| A_{in} \Delta t_{rec} < V_{bc}$, the inlet tracers will move during Δt_{rec} and end to those (neighboring-) cells, with a normal physical behavior.

However, when $V_{tr}^{inlet} = \epsilon_{s/g}||\boldsymbol{u}_{in}||A_{in}\Delta t_{rec} > V_{bc}$, which occurs at significant inlet velocities or long Δt_{rec}, a big portion of the inlet tracers will travel deep inside the domain and they will all end to one cell producing unphysical high accumulation hit of transported concentration. In this regard, a temporal delaying approach on these tracers, by random periods between [0: Δt_{rec}], is required in order to distribute them homogeneously along its path next to the inlet. Regarding the outlet flux, we respect to those internal tracers that hit the outlet surfaces, A_{out}, and leave the domain in each Δt_{rec}, as outlet tracers. If we count these tracers each time step Δt, as N_{tr}^{outlet}, hence their volumes can be set to $V_{tr}^{outlet} = \epsilon_{s/g}||\boldsymbol{u}_{out}||A_{out}\Delta t/N_{tr}^{outlet}$ (see the corresponding subset of Step (4) in Figure 2). Finally, at the end of τ_{rec}, the stored database ends up to grouped information positions of start–end internal tracers, end inlet tracers, and start outlet tracers, for each Δt_{rec}.

At this stage, the short-term full CFD simulation is stopped and the offline passive transportation can be triggered on the base of the stored data set and the recurrent sequence control. It achieves a time-extrapolating prediction of a passive scalar concentration traced on recurrent moments, and enduring till eternity. The offline transportation steps are graphically pictured in Figure 2, where, in this context, we shortly outline them as following:

1. Transport the inlet concentration γ_c^{inlet}, pursuing the stored shift positions of the inlet tracers. In case of facing multiple transportations in the same end grid cell a weighted average is applied as

$$\gamma = \frac{\sum_{i=1}^{hits} v_{inlet}^{i}\gamma_c^{inlet}}{\sum_{i=1}^{hits} v_{inlet}^{i}}, \quad \text{with} \quad i = 1,2,\ldots,\text{hits}, \tag{5}$$

where v_{inlet}^{i} is the volume of inlet tracer.

2. Transport the concentration γ following the shift positions of internal tracers. Likewise, for cells of more than one shift operation and, for instance, the cell is hit by an inlet tracer, γ is given as

$$\gamma = \frac{\left(v_{inlet}\gamma_c^{inlet} + \sum_{i=1}^{hits}\epsilon_{s/g}^{i}v_{tr}^{i}\gamma_{c_i}\right)}{\left(v_{inlet} + \sum_{i=1}^{hits}\epsilon_{s/g}^{i}v_{tr}^{i}\right)}, \quad \text{with} \quad i = 1,2,\ldots,\text{hits}, \tag{6}$$

where v_{tr}^{i} is the volume of internal tracer and γ_{c_i} is the concentration transported from the cell c_i, with the volume fraction $\epsilon_{s/g}^{i}$ (following the phase on which the propagation of passive scalar is traced).

3. Fill the holes. Meaning that, those resultant cells which are not hit by any transport information, its value will be interpolated by the surrounding cells concentration.
4. Consider the concentration of the start-cell outlet tracers as γ_c^{outlet}. Meaning that, the concentration in the cells where the outlet tracers were located at the beginning of Δt_{rec}, and before leaving the domain.
5. One step correcting diffusion controlled by the physical global balance between the coming-in, accumulated, and going-out mass concentration in the total domain,[32] that is,

$$\frac{Dm_\gamma}{dt} = \frac{dm_\gamma}{dt} + \nabla\cdot\left(\boldsymbol{u}_{s/g}\gamma\right) = 0 \int\int \Rightarrow m_\gamma^{t+\Delta t_{rec}} = \left(\dot{m}_{\gamma_{in}} - \dot{m}_{\gamma_{out}}\right)\Delta t_{rec} + m_\gamma^{t}, \tag{7}$$

and which can be written as

$$\sum_{i=1}^{cells}\left(\epsilon_{s/g}^{i}\gamma_{c_i}V_{cell}\right)^{t+\Delta t_{rec}} = \sum_{i=1}^{inlet} v_{inlet}^{i}\gamma_{c_i}^{inlet} - \sum_{i=1}^{outlet} v_{outlet}^{i}\gamma_{c_i}^{outlet} + \sum_{i=1}^{cells}\left(\epsilon_{s/g}^{i}\gamma_{c_i}V_{cell}\right)^{t}. \tag{8}$$

If the left-hand side (LHS) in Equation (8) exceeds the target (right-hand side RHS), the diffusion operator loops over all the internal faces and shifts/swaps rigorously (out) a specific concentration portion from the high-concentration cell, as

$$\Delta\gamma = f\frac{\gamma_{c_i} - \gamma_{c_{i+1}}}{2}. \tag{9}$$

Here, c_i and c_{i+1} are the two adjacent cells which share the surface, and f is a constant diffusion factor of magnitudes $1/2^n$. In the contrary case, when the system indicates an excessive target the shift direction will be (in) toward the low-concentration cells.

In different than the previous transport-based rCFD version reported in Reference,[32] the aforementioned methodology implicates physically consistent enhancements regarding the inflow and outflow modelings. Namely, the inflow modeling before was by setting a concentration source next to the inlet and convey it following the internal tracers. Therefore, in some situations when the portion of these tracers is insufficient, a discontinuity in the concentration transport can be produced. On the other hand, the outflow was globally aligned to a *constant* value of the inflow, and was uniformly distributed over the outlet adjacent cells. In this case, the going-out mass concentration is roughly approximated with no local accuracy. All these features are resolved in the current version to make the methodology more consistent and associated totally to the particles dynamics. The functionalities therein besides the incoming experienced diffusion are implemented in the frame of user-defined functions code in the software ANSYS/Fluent.

3 | RESULTS AND DISCUSSION

We consider the simulation of a lab-scale (Geldart B particle) bubbling fluidized bed, displayed in Figure 3a, within the framework of the

following separated cases. First, introduce a mixture of two species on the gas phase by injecting a red-color species into the lateral gas inlet and a blue-color species into the bottom gas inlet. Second, set an initial mixture of a red-color (small rectangular region) and blue-color (elsewhere) species, on the solid phase (Figure 3c). Third, consider the enthalpy transport with an initial hot rectangular region of the solid phase, that is, T_s = 500 K (Figure 3d), and a continuous cold air, that is, T_g = 300 K, passing within all air inlets.

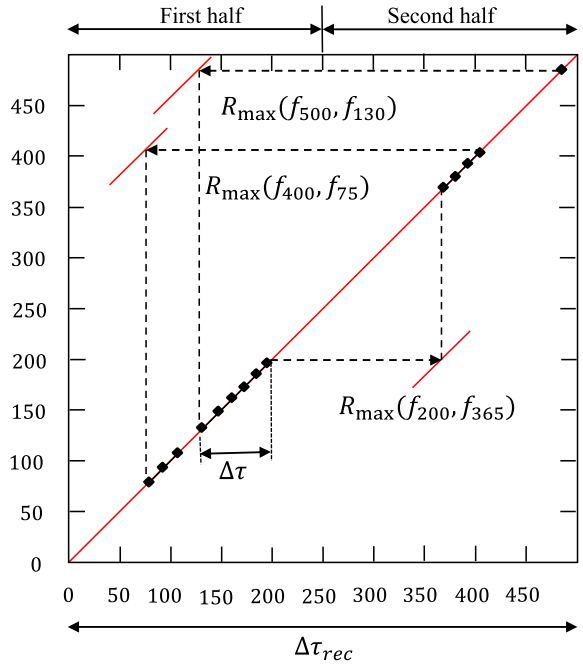

FIGURE 1 Sketch of the recurrence path construction strategy, where the off-diagonal red lines correspond to the maximal recurrence norm [Color figure can be viewed at wileyonlinelibrary.com]

To do so, the mathematical models described in Section 2.1 and Appendix are numerically resolved in Cartesian coordinates $\boldsymbol{r} = (x, y, z)$, using a uniform hexahedral grid and adopting the Eulerian multiphase model available by ANSYS/Fluent code. We mainly seek the proper application of the transport-based rCFD model in fluidized bed, so we settle with an acceptable grid size $\Delta \boldsymbol{r}_i = 2.57 \times 10^{-3}$ m $\sim 5d_s$[35] (five times the grain diameter), for a reactor geometry {x = (–0.009375:0.009375) m, y = (–0.074:0.074) m, z = (0:0.4) m}, that captures well all relevant heterogeneities in the framework of TFM large-scale approach. The selected dimensions correspond to our local experimental setup that allows us an optical accessibility in such future experiments. Regarding the numerical methods, a finite-volume first-order upwind scheme is adopted for the spatial discretization of all convective terms in the governing equations (Equations A1, A8, A14, and A15). The temporal discretization, by turn, follows the first-order backward difference scheme and implicit integration in the time derivatives and leading terms, therein. To solve the phasic velocity–pressure coupling, the phase-coupling SIMPLE algorithm available in ANSYS/Fluent for multiphase flows is employed. Therein, the velocities are solved and coupled by phases in a segregated fashion; while the fluxes are reconstructed at the faces of the control volume to correct the pressure, afterward, on the base of the total continuity. The coefficients of the pressure correction equations come from the coupled per phase momentum equations, and the final linear system is resolved using the multigrid method. For details about the numerical methods, algorithms and solver, the reader is referred to.[36] The consistent time step Δt is defined by an appropriate value $\Delta t = 5 \times 10^{-4}$ s, which satisfies the Courant number Co = $\boldsymbol{u}_g \Delta t / \Delta \boldsymbol{r} \leq 0.1$, at the operating conditions. We firstly run

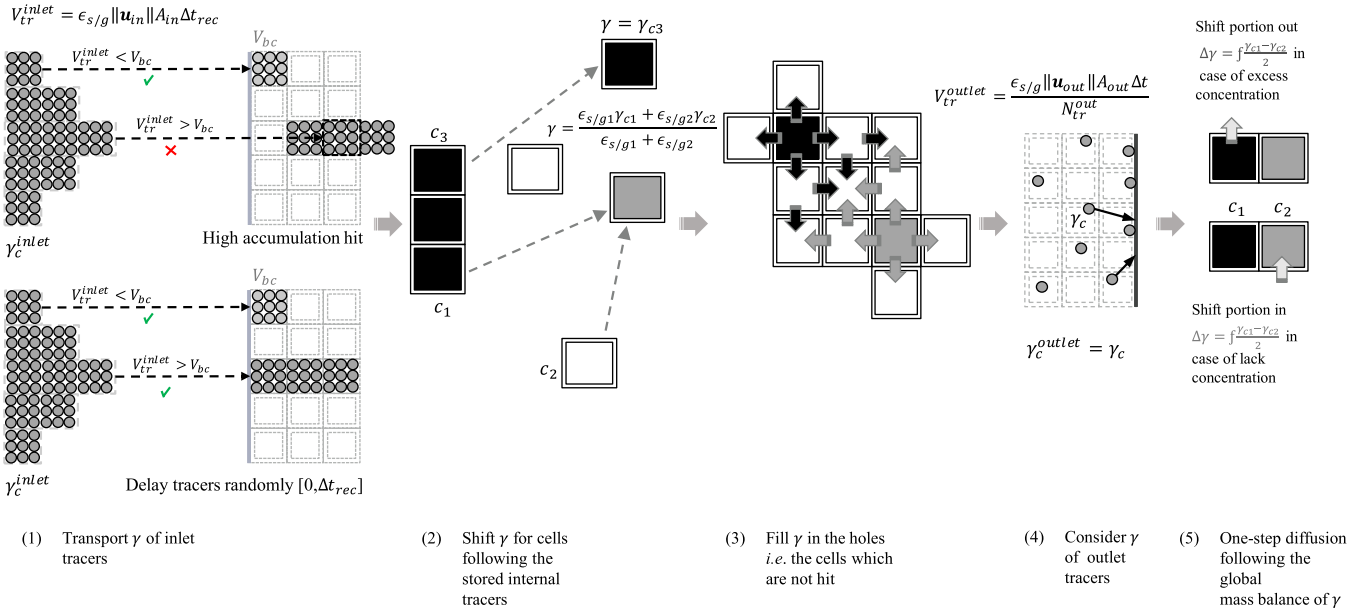

FIGURE 2 Informative graphics on the transport-based recurrence computational fluid dynamics methodology [Color figure can be viewed at wileyonlinelibrary.com]

the simulation an initial period of τ_{initial} = 3 s that ensures the starting of bubbles formation and the (pseudo) periodicity of the system, at which all initial transient effects are certainly washed out. Afterward, the evolution of various fields such as, the pressure p, the solid vertical velocity w_s, and the solid volume fraction ϵ_s, at a central probing point, ◊(0, 0, 0.05), inside the bed, is monitored in

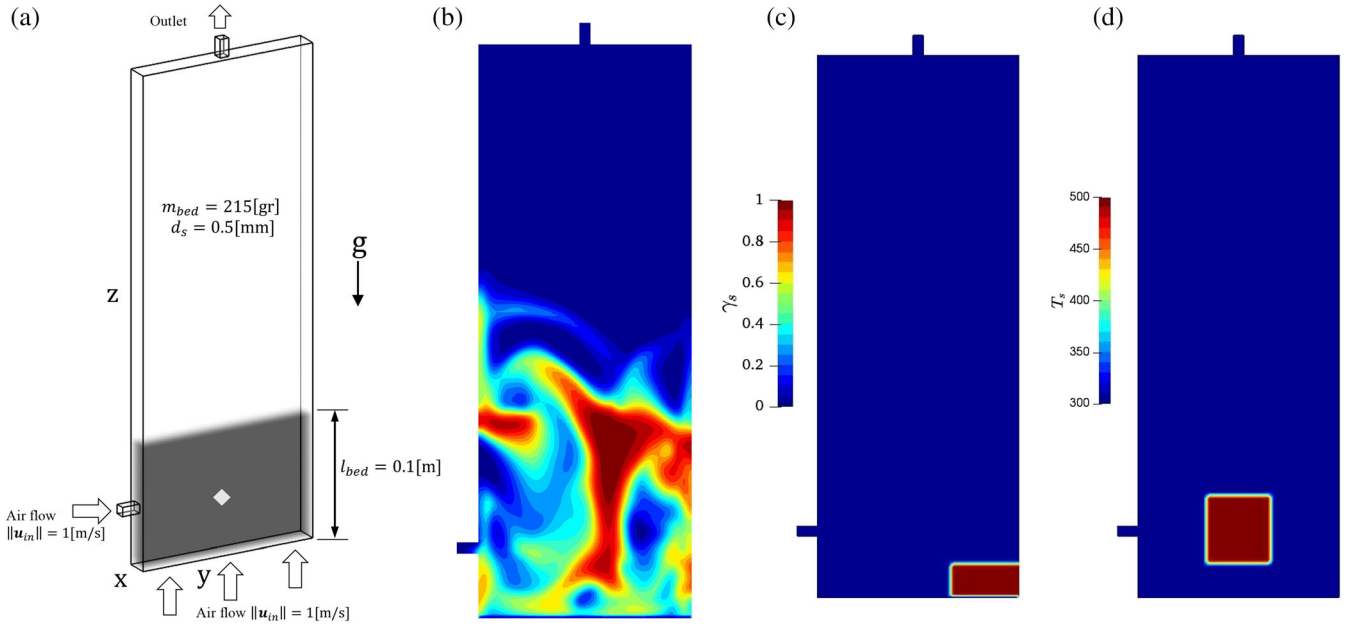

FIGURE 3 (a) A schematic representation of the simulated fluidized bed of dimensions ~2 cm × 15 cm × 40 cm. Air enters through lateral and bottom inlets, with the infusion of red-color and blue-color species, respectively. It fluidizes the solid particles (dark volume) and leaves the domain through a shrank outlet at the top. All the walls of the domain are imposed to be no-slip boundaries and the diamond symbol ◊(0, 0, 0.05), represents the probing point considered. (b) An instantaneous mid-width picture of ϵ_s, in red, that corresponds to the isolating moment n = 250 on $R^{(\epsilon_s)}$ matrix, while (c) and (d) expose the initial conditions of species and temperature on the solid phase, respectively [Color figure can be viewed at wileyonlinelibrary.com]

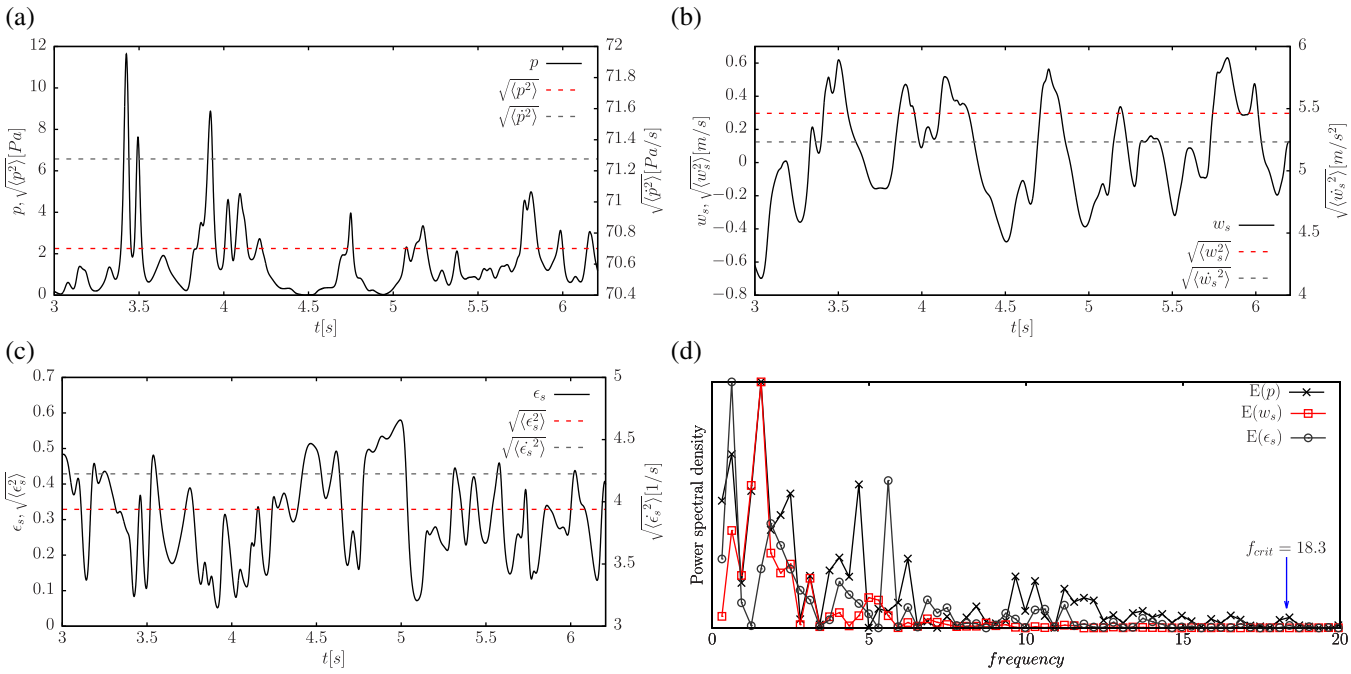

FIGURE 4 Probe values of (a) pressure, (b) z-component solid velocity, and (c) solid volume fraction, at the sampling point ◊(0, 0, 0.05), together with their average quantities. (d) The energy value of Fourier components including the minimum critical frequency, that is, lowest-lying peak that has to be exceeded to enable useful recurrence statistics [Color figure can be viewed at wileyonlinelibrary.com]

Figures 4a–c, together with its average and spectral analysis (Figure 4d). They have been utilized, a priori, to decide the recurrence properties, that is, Δt_{rec} and τ_{rec}, given by Equation (1) and (2), respectively.

Following the mean-square values and temporal derivatives, the variational quantities indicate, $\sqrt{\langle p^2\rangle/\langle \dot{p}^2\rangle}\approx 0.03\,\text{s}$, $\sqrt{\langle w_s^2\rangle/\langle \dot{w}_s^2\rangle}\approx 0.056\,\text{s}$ and $\sqrt{\langle \epsilon_s^2\rangle/\langle \dot{\epsilon}_s^2\rangle}\approx 0.077\,\text{s}$, for p, w_s, and ϵ_s, respectively. Using the aid of different similar analyzing points, not shown here, the consistent value is decided as $\Delta t_{\text{rec}} = 0.008\,\text{s}$, that resolves adequately the global pseudoperiodic characteristics. All simulation details and recurrence properties are summarized in Table 1, where $\tau_{\text{rec}} = \tau_{\text{rec}}^{\gamma_g}$, is identified for the period used in the gaseous species modeling, while $\tau_{\text{rec}}^{\gamma_s}$ and τ_{rec}^{T} are defined for those periods in the solid species and temperature transport, respectively. In different than the case of continuous coming-in gaseous species, the solid species and heat transfer problems are set by an initial value, as a small rectangular region, for the solid mass fraction and solid temperature. In the solid species problem, this initial mass fraction (unity) will be diffused in time till the reach of the uniform concentration. Hence, in order to avoid this final attainment, $\tau_{\text{rec}}^{\gamma_s}$ is decided shorter than in the gaseous species. Likewise, in the temperature transport problem, the heat will be transfered inside the solid phase itself and toward the gas phase. This last in turn, is continuously going-out through the outlet, and thus τ_{rec}^{T} is selected shorter in order to avoid the uniform cold extent.

During the full CFD τ_{rec} simulation, the fields of solid fluxes and volume fraction are stored each $\Delta t_{\text{rec}} = 16\Delta t$, to eventually obtain 400 flow frames. The recurrence matrices (Equation 4) are then constructed upon the recurrence norm (Equation 3), and shown in Figures 5a,b, for $R^{(\epsilon_s)}$ and $R^{(\epsilon_s \boldsymbol{u}_s)}$, respectively. Following the

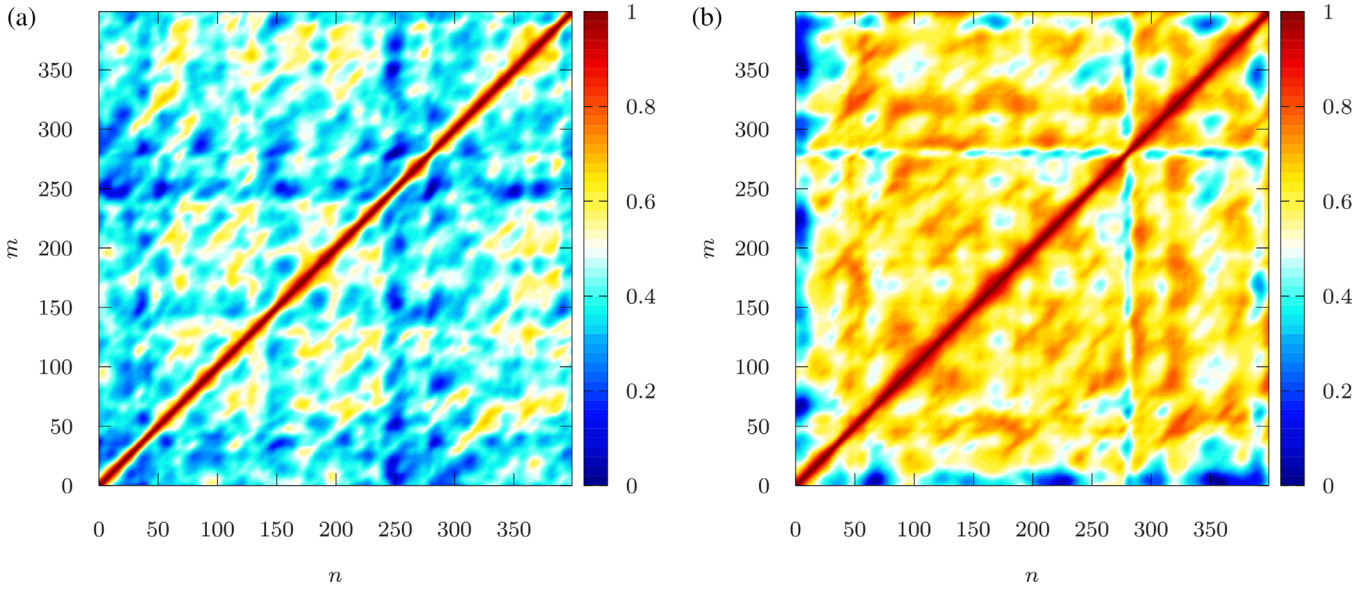

FIGURE 5 Plots of recurrence matrix constructed upon the recurrence norm: (a) $R^{(\epsilon_s)}$ and (b) $R^{(\epsilon_s \boldsymbol{u}_s)}$ [Color figure can be viewed at wileyonlinelibrary.com]

TABLE 1 Summary of the fluidized bed simulation parameters and recurrence properties

	Property	Value	Unit	Simulation details	Value	Unit
Gas density	ρ_g	1.2	kg/m^3	N_{cell}	66,000	V_{cell}
Solid density	ρ_s	1,400	kg/m^3	V_{cell}	1.7×10^{-8}	m^3
Species density	$\rho_{j_{1,2}}$	1.2	kg/m^3	Δr_i	2.57×10^{-3}	m
Grain diameter	d_s	0.5	mm	τ_{initial}	3	s
Thermal conductivity	$\kappa_s = \kappa_g$	0.0242	W/m K	$\tau_{\text{rec}} = \tau_{\text{rec}}^{\gamma_g}$	3.2	s
Gas viscosity	μ_g	1.79×10^{-5}	kg/m s	Δt	5×10^{-4}	s
Bed mass	m_{bed}	215	g	Δt_{rec}	0.008	s
Initial bed height	l_{bed}	0.1	m	$\|\|\boldsymbol{u}_{\text{in}}\|\|$	1	m/s
Species diffusivity	$D_{j_{1,2}}$	2.88×10^{-5}	m^2/s	N_{tr}	{70,000, 10^6}	Tracer
Gas specific heat	c_p^g	1,006.42	J/kg K	$\tau_{\text{rec}}^{\gamma_s}$	1.6	s
Solid specific heat	c_p^s	840	J/kg K	τ_{rec}^{T}	1.6	s

deep fluctuated pressure, the solid flux $\epsilon_s \boldsymbol{u}_s$, reveals a coherent relevance to the uniform flow periodicity (note the signal of w_s in Figure 4b). Namely, it highly discloses the fingerprints of rising bubbles passage, with high effective solid mixing through the wake effect particles, emulsion drift particles, and the bubble eruptions particles.[37] The gas flow, however, evolves as dense flow in rich solid areas, visible bubbles, and throughflow which bypasses through the bubbles.[38] Hence $\epsilon_g \boldsymbol{u}_g$ includes high fluctuated dynamics that absentees the recurrence between states and can be less appropriate for the periodicity disclosure.

The volume fraction, $\epsilon_{s/g}$, in turn, stands to be a strong and directly sensitive field to the bubbles identification, where its recurrence norm value is identical for the gas and solid phases, $R^{(\epsilon_s)} \equiv R^{(\epsilon_g)}$. Looking at the recurrence matrices in Figure 5, one can notice the run of irregular off-diagonal patterns, parallel to the diagonal, and remarked by local minima and maxima of recurrence norm. They indicate a well-similar evolution of flow repeated over some time and endures relatively over few Δt_{rec}, in corresponding to the frequency of the bubbles emission. Both recurrence matrices possess approximately similar fingerprint structures that can differ by the evolution moments. For instance, the isolating moment n = 250 on $R^{(\epsilon_s)}$ matrix and which corresponds to an unusual big bubble expanded across the bed (see the matching snapshot in Figure 3b), has its sign on $R^{(\epsilon_s \boldsymbol{u}_s)}$ matrix at $n \sim 276$. At the end, the two R matrices are connected and well representative.

3.1 | Reconstruction of species transport on gas phase

In this context, we continue the rCFD application by assessing the enhanced methodology of transport-based rCFD model (Figure 2) for the reproduction of gaseous species transport all along $\tau_{rec}^{\gamma_g}$. In other words, the tracer-based shift information of $N_{tr} = 10^6$ tracers, linked to the gas dynamics, and stored for 400 flow frames are retrieved in sequential order, that is, the recurrence path is $\{f_1, f_2, \ldots, f_{400}\}$. The offline steps outlined in Section 2.2 are applied in correspondence, to transport a passive scalar with boundary inputs as, the lateral red-color concentration, $\gamma_c^{inlet} = 1$, and the bottom blue-color concentration, $\gamma_c^{inlet} = 0$. By this way, we mimic the transport of the two species mass fraction injected, with a time step $\Delta t_{rec} = 16\Delta t$. The key feature is about how to properly calibrate the correcting diffusion Step (5), after the ill-conservative convection procedure accomplished in Steps (1), (2), and (3). Its error implicates compensative diffusion effects coming from the physical molecular diffusion in part, and the fluctuated walk that species undergo along its path Δt_{rec}. Let us say the integral diffusion regarding to the temporal filtering with Δt_{rec}. In addition to these physically based sources, a numerical error can also come from the interpolated impartation of concentration in filling the holes Step (3). In this regard the error can be reduced by using a sufficient number of tracking tracers N_{tr} that ensures the (hit) transportation for most of the grid cells. Hence, the face-swap diffusion operator is implemented in the framework of two objectives.

3.1.1 | Global mass species conservation

Following the global conservation condition of integral mass concentration over Δt_{rec}, and which is given in Equation (7), the face-swap concentration $\Delta\gamma$ (Equation 9) between two cells, is passed in or out, as explained in Step (5). Note that this criterion is physically based and comprehensive to correct the mass balance deviation in local-careless way. Talking in global sense, the diffusion amount needed can notably vary between flow frames, in relevance to the species lifetime that is essentially associated to the gas dynamics (i.e., ϵ_g, $\epsilon_g \boldsymbol{u}_g$). Therefore, instead of using a constant diffusion factor f, its value is defined in an approximate dynamical way. Namely, given an upper, $1/2^3$, and lower, $1/2^7$, bound, the value of the diffusion factor is increasing/decreasing if the RHS of Equation (7), tends to be bigger/smaller than the LHS, from one frame to the next. Following that attitude, the diffusion procedure is applied standalone in only one loop step for each frame, and the pertinent outcomes have revealed a feasible chasing to the actual full CFD species simulation. For example, by considering a visual instantaneous comparison (at t = 6.2 s) between the full CFD results and rCFD, as shown in Figures 6a, one can observe the good tracing using very short runtime; however, an excess of the concentration transported is sustained (Figure 6a, middle). This excess is clearly pronounced in the evolution of the global mass quantity, that is, $m_\gamma = \sum_{i=1}^{cells} \left(\rho_g \epsilon_g^i \gamma_{c_i} V_{cell} \right)$ computed all along $\tau_{rec}^{\gamma_g}$, and represented in Figure 6b (bottom). Therein, the rCFD results indicate a higher concentration than it is out to be in the mass fraction species. In a detailed review, as well, the high concentration is remarked on γ histogram chart generated for the same instant in Figure 6a and displayed in Figure 6b (top). The frequency, therein, is shown in a logarithmic scale in order to highlight the few high γ distribution.

On the basis of that, one can conclude that applying one loop diffusion standalone cannot return the proper diffusive consequences even though it is a very fast procedure from practical point of view. Another approach is sought in the same line by doing multiple diffusion loops till the convergence between the two sides in Equation (7). For the sake of quickness and simplicity, the diffusion factor is chosen as a constant value, that is, $f = 1/2^9$, which is proportional to the molecular diffusion coefficient, that is, $f \approx D_j \Delta t / A$. It has to be certainly smaller than the lower bound in the dynamical procedure above, where A here is supposed to be the face area through which the concentration swapping takes place. This factor contributes into the molecular diffusive part, and by repeating it several times in consistency with the mass balance converging, the proper amount of diffusion in each particular frame will be recovered. Each frame requires a different number of diffusion loops to eventually make the approach somewhat expensive (see the performance Figure 16a in Section 3.5). If we explore the same mere optical comparison in Figure 6, the new outcomes, referred as confined molecular diffusion, give a subtle capturing to the actual full CFD evolution in instant (Figures 6a, right) and global (Figure 6b, bottom) terms. They deliver a nice reproduction to the species path, but in such locally rough transport. Looking closely, the procedure relatively dissipates the concentration in some regions,

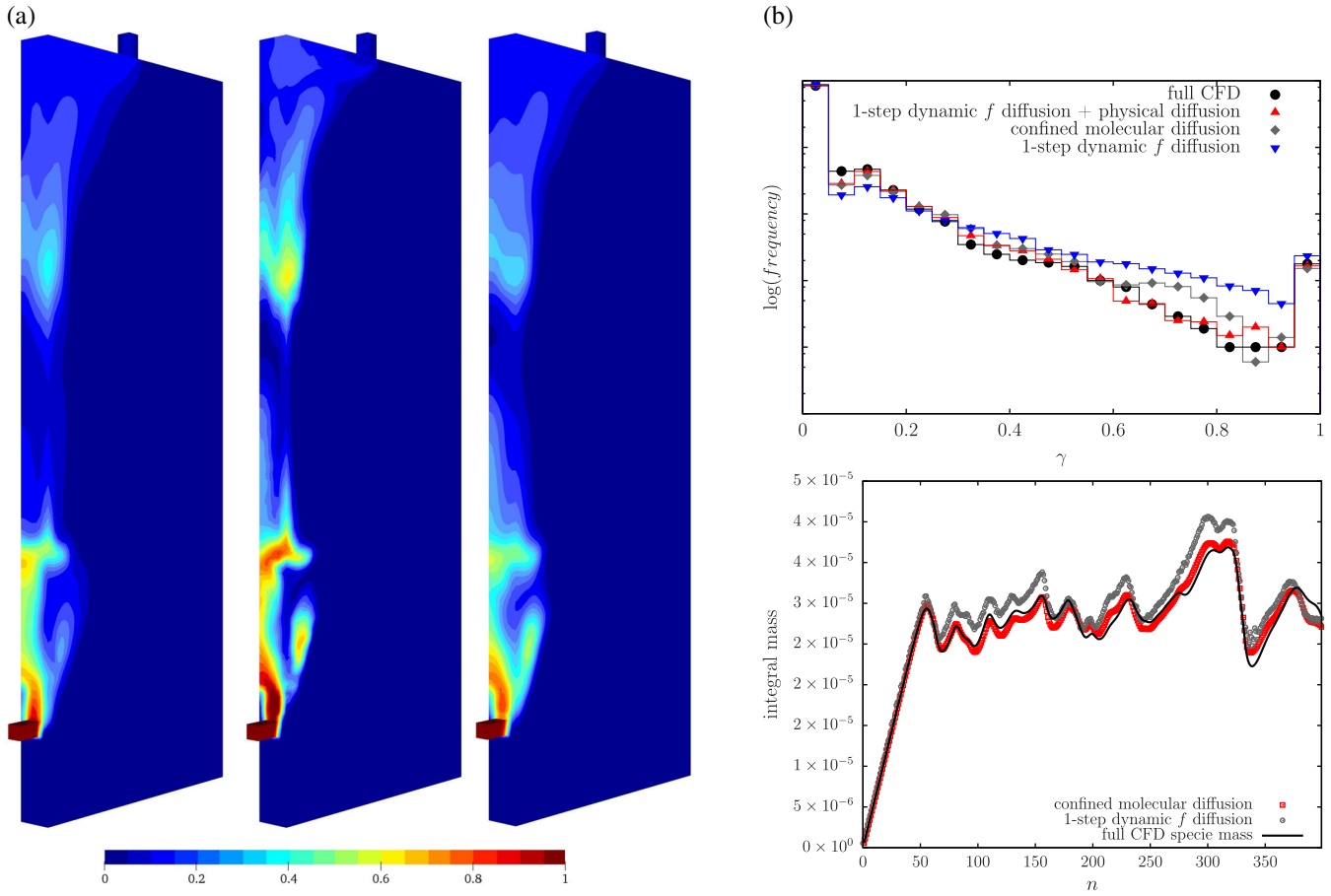

FIGURE 6 (a) Comparative instantaneous pictures (t = 6.2 s) between the actual full computational fluid dynamics (CFD) red-color specie simulation (left) and recurrence CFD (rCFD) reconstructed concentration using one dynamical f diffusion loop (middle) and multiple constant f diffusion loops, as the confined molecular diffusion (right). (b) At the top, shows the histogram of concentration for the pictures presented in (a) in addition to the rCFD outcomes, for the same moment, using the local diffusion (shown in Figure 8a, right). The frequency of the histogram is demonstrated in a logarithmic scale. (b) At the bottom, exposes the evolution of the global mass quantity of concentration results experienced in (a). All rCFD outcomes are obtained using $N_{tr} = 10^6$ [Color figure can be viewed at wileyonlinelibrary.com]

for instance, outside of the bed, more than what is out to do. While, in other parts close to the source, the operator does not dissipate sufficiently. Note the histogram, particularly, in Figure 6b (top). Finally, these globally controlled models are feasible in terms of the main purpose of rCFD and saving considerable computational effort, but in spite of that a better calibration using a local diffusion is somehow mandatory.

3.1.2 | Local diffusion

In order to derive, accurately, all compensative diffusion effects, we firstly execute a one globally controlled diffusion loop characterized by a dynamical determination of the diffusion factor (see Section 3.1.1). This step satisfies an initial correction to the methodology's error in a featureless global way. Then we follow it by a kind of a fast and local physical diffusion approach. To that end, the oscillated (random) walk of species parcel along its path, from the beginning to the end Δt_{rec}, is assumed as a turbulent diffusion and computed on the base of the turbulent kinetic energy of the tracked tracers. Taking the online temporal sampling of tracers velocity fluctuations $\boldsymbol{u}'_p$, that is, velocity variance, during Δt_{rec}, the turbulent kinetic energy results as

$$k = \frac{1}{2}\left(\left\langle u_p'^2\right\rangle + \left\langle v_p'^2\right\rangle + \left\langle w_p'^2\right\rangle\right). \tag{10}$$

The sample variance of each velocity component, as a scalar $\langle \varphi'^2 \rangle$, is computed in online running way. Namely, we adopt a fast and cheap algorithm for evaluating the running variance directly at the same arrive moment without the need to save data for a second pass.[39] The method implies calculating of two variants, that is, M and S, for each individual tracer, and which are being updated each particle time step along Δt_{rec}. Giving initial values, $M_1 = \varphi_1$ and $S_1 = 0$, the subsequent i moment for these quantities is computed as

$$M_i = M_{i-1} + \frac{(\varphi_i - M_{i-1})}{i} \quad \text{and} \quad S_i = S_{i-1} + (\varphi_i - M_{i-1})(\varphi_i - M_i), \tag{11}$$

for $2 \le i \le n_p$, where n_p is the accumulated number of particle/tracer time steps along Δt_{rec}. Finally, the variance value ends to $\langle \varphi'^2 \rangle = S_{n_p}/(n_p - 1)$, and stored as an auxiliary parameter in the tracers database. After figuring the turbulent kinetic energy k (Equation 10), the consequential turbulent diffusion is estimated by a mixing length model,[40] that is,

$$D_j^t = \frac{\nu_j^t}{Sc_t}, \text{ with } \nu_j^t = C\Delta k^{1/2}. \tag{12}$$

Therein, C is an empirical constant, while $Sc_t = 0.7$ is the turbulent Schmidt number and $C\Delta = C(\Delta x \Delta y \Delta z)^{1/3}$ is the deterministic mixing length scale. Roughly speaking, this is basically identical to the suggestion of Kolmogorov and Prandtl (see references in Pope[40]) for approaching the turbulent viscosity ν_j^t in the frame of the gradient-diffusion hypothesis and Reynolds-averaged Navier–Stokes fluid turbulence models. In our case, we neither model any unresolved small scale fluctuations linearly aligned with the gradient of mean γ, nor resolve any empirical k-equation in order to close the system; we only estimate the accumulated possible diffusion of species along Δt_{rec}, following the tracers dynamics. By summing up this temporal coarsening amount, D_j^t, to the molecular diffusion part, D_j, the consecutive local physical diffusion step can be given as

$$\Delta\gamma = \left(D_j + D_j^t\right) \frac{\gamma_{c_{i+1}} - \gamma_{c_i}}{\Delta \boldsymbol{r}_{c_i,c_{i+1}} \cdot \boldsymbol{n}_A} A\left(\frac{\Delta t_{rec}}{V_{cell}}\right), \tag{13}$$

passing in γ_{c_i} and out $\gamma_{c_{i+1}}$. Here, $\Delta \boldsymbol{r}_{c_i,c_{i+1}}$ is the vector distance from c_i to c_{i+1} and $\boldsymbol{n}_A$ is the surface-normal vector on the same direction. Probing different constants C in Equation (12), with a special near-wall treatment, that is, $\Delta = 0.5V_{cell}^{1/3}$, the tests are demonstrated in Figures 7 and 8, together with the outcomes of the previous approaches. In global-scale investigations, the suitable concentration modeling has suggested a constant value of $C = 0.2$, that best fits the full CFD evolution (Figure 7a), Therewith, the new evolution of the global mass shows identical behavior to the confined molecular diffusion by performing only two diffusion loops (one dynamical + one physical), to eventually be a very economic procedure (see the performance Figure 16a in Section 3.5).

On the other hand, the instant reproduction of species structures is enhanced using the new strategy, as can carefully be noticed in Figures 8a. It relatively gives better following than the confined approach (see the histogram in Figure 6b, top), as well on the mean fields shown in Figure 8b. Therein, the mid-width profiles of $\langle \gamma \rangle$, averaged over all frames, and extracted at the lines (0, y, z = {0.04, 0.08, 0.1, 0.2, 0.3}), are mapped. One can note how the new procedure can accurately capture the full CFD species distribution even in very low concentration regions, for example, at $z = 0.04$. In conclusion, the enhanced local diffusion comes to be the reliable and most feasible approach for the fast methodology of transport-based rCFD.

3.2 | Reconstruction of species transport on solid phase

In this problem, and identical to the reproduction procedure of gaseous species transport, the Lagrangian shift information of $N_{tr} = 10^6$ tracers, linked to the solid dynamics, and stored for 200 flow frames ($\tau_{rec}^{\gamma_s}$), are retrieved in sequential order. Following the offline Step (2.2),

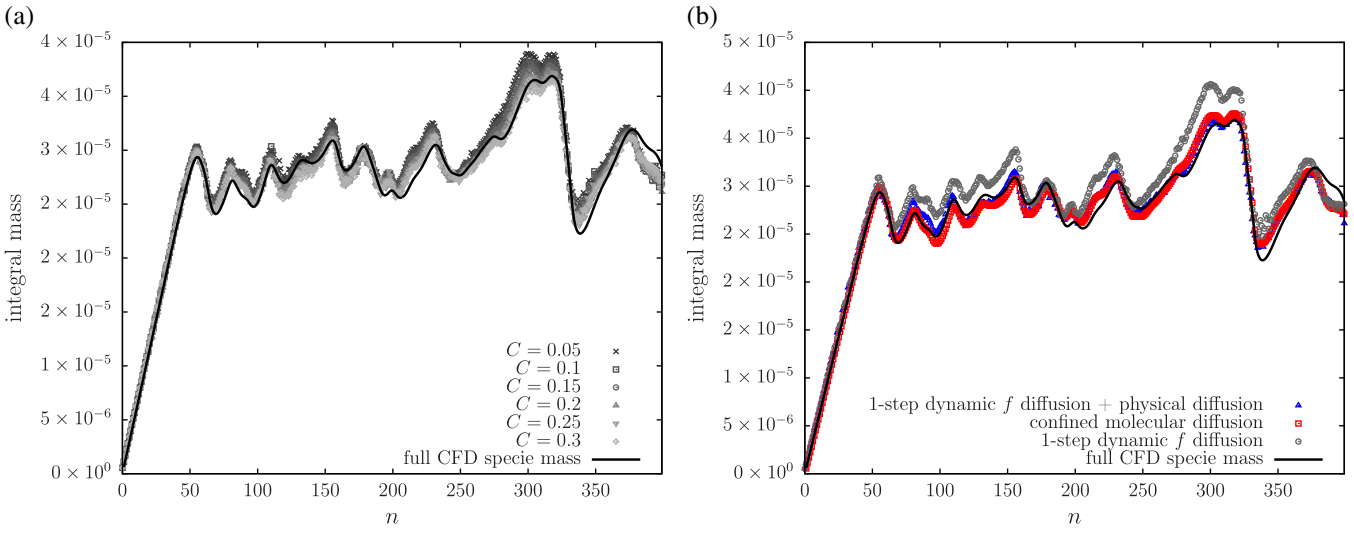

FIGURE 7 (a) The assessed evolution of global mass recurrence computational fluid dynamics (rCFD) concentration using the local diffusion approach, and probing different C values in Equation 12. (b) The same Figure 6b (bottom), with adding the rCFD local diffusion evolution ($C = 0.2$). All rCFD outcomes are obtained using $N_{tr} = 10^6$ [Color figure can be viewed at wileyonlinelibrary.com]

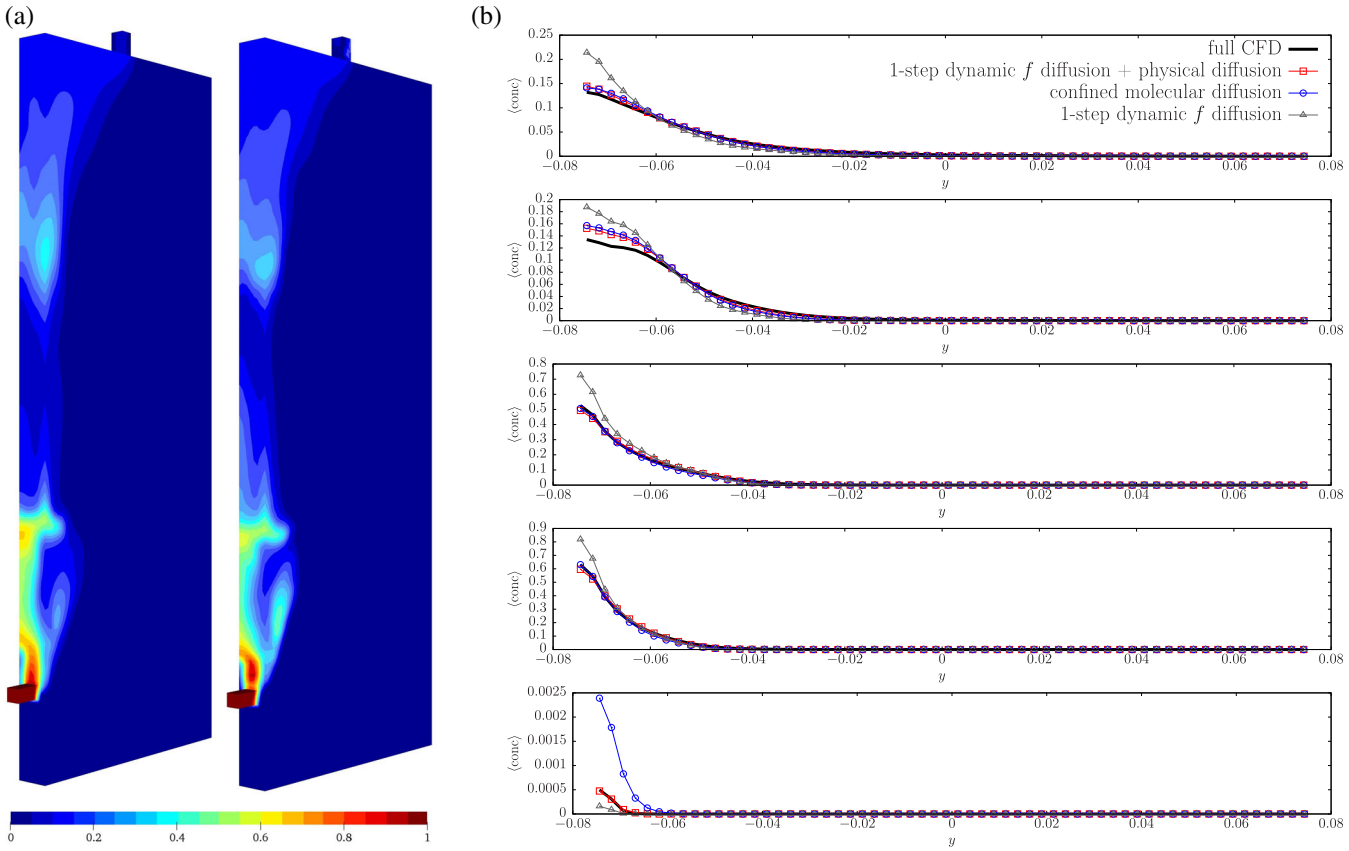

FIGURE 8 (a) Comparative instantaneous pictures (t = 6.2 s), similar to Figure 6a, for the full computational fluid dynamics (CFD) species simulation (left) and recurrence CFD (rCFD) reconstruction (right), adopting the local diffusion approach (C = 0.2). (b) The corresponding resultant mean profiles, extracted at (0, y, z = {0.04, 0.08, 0.1, 0.2, 0.3}), from bottom to top, respectively, and gotten following the confined molecular diffusion, dynamic f diffusion and the local diffusion approaches (C = 0.2). All rCFD outcomes are obtained using $N_{tr} = 10^6$ [Color figure can be viewed at wileyonlinelibrary.com]

the transportation starts with an initial imposed rectangular red-color passive scalar, quite identical to the full CFD simulation conditions. Then, the proper local diffusion approach, outlined in 3.1.2, is employed, as well, for solid species transportation. Therein, the physical diffusion step is fetched by Equation (13), and the molecular solid diffusivity, here, is considered constant and equivalent to the gas phase.

Because the injected tracers in this problem chase the solid velocities, which account to smaller magnitudes than the gas phase, the sampling turbulent kinetic energy k becomes lower. And, in consequence, the turbulent diffusion (Equation 12) requires a higher value for the empirical constant, which is found to be suitable by C = 0.8. By doing so, a feasible reconstruction of solid species structures is obtained using a cheap and short runtime computations (see the performance Figure 16b in Section 3.5). On the other hand of an optical instant comparisons, two moments, at the beginning, t = 3.16 s, and the end t = 4.6 s, of $\tau^{\gamma_s}_{rec}$, are mapped in Figure 9 for the field ($\epsilon_s\gamma$). It can be noticed an acceptable matching between the rCFD results and full CFD counterparts. Moreover, the mid-width profiles, averaged over 200 flow frames, for $\langle\epsilon_s\gamma\rangle$, and extracted inside the bed, at positions (x = 0, y, z = {0.01, 0.02, 0.03, 0.04, 0.05, 0.06, 0.07, 0.08, 0.09} m), have revealed a satisfied rCFD modeling, as represented in Figure 10.

3.3 | Reconstruction of heat transport

Different than the previous offline rCFD methodology, which predicts the transport of *standalone*-phase species, the heat transfer, herein, sustains an interaction between the gas and solid phase. In order to capture this interaction, the values of heat transfer coefficient Nu are computed during the online tracking procedure, that is, τ^{T}_{rec}, beforehand, and stored as an auxiliary online data. In that stage, both the gas and solid dynamics are simultaneously tracked by injecting two groups of $N_{tr} = 5\times10^5$, massless tracers, to eventually produce two shift information data sets. Afterward, the reconstructed transportation of T_g and T_s scalars with the selfsame full CFD initial conditions is commenced in the framework of the following modified rCFD algorithm:

1. Transport T_g following the inlet gas tracers shift positions, and employing a two-halfs temporal integration step for the

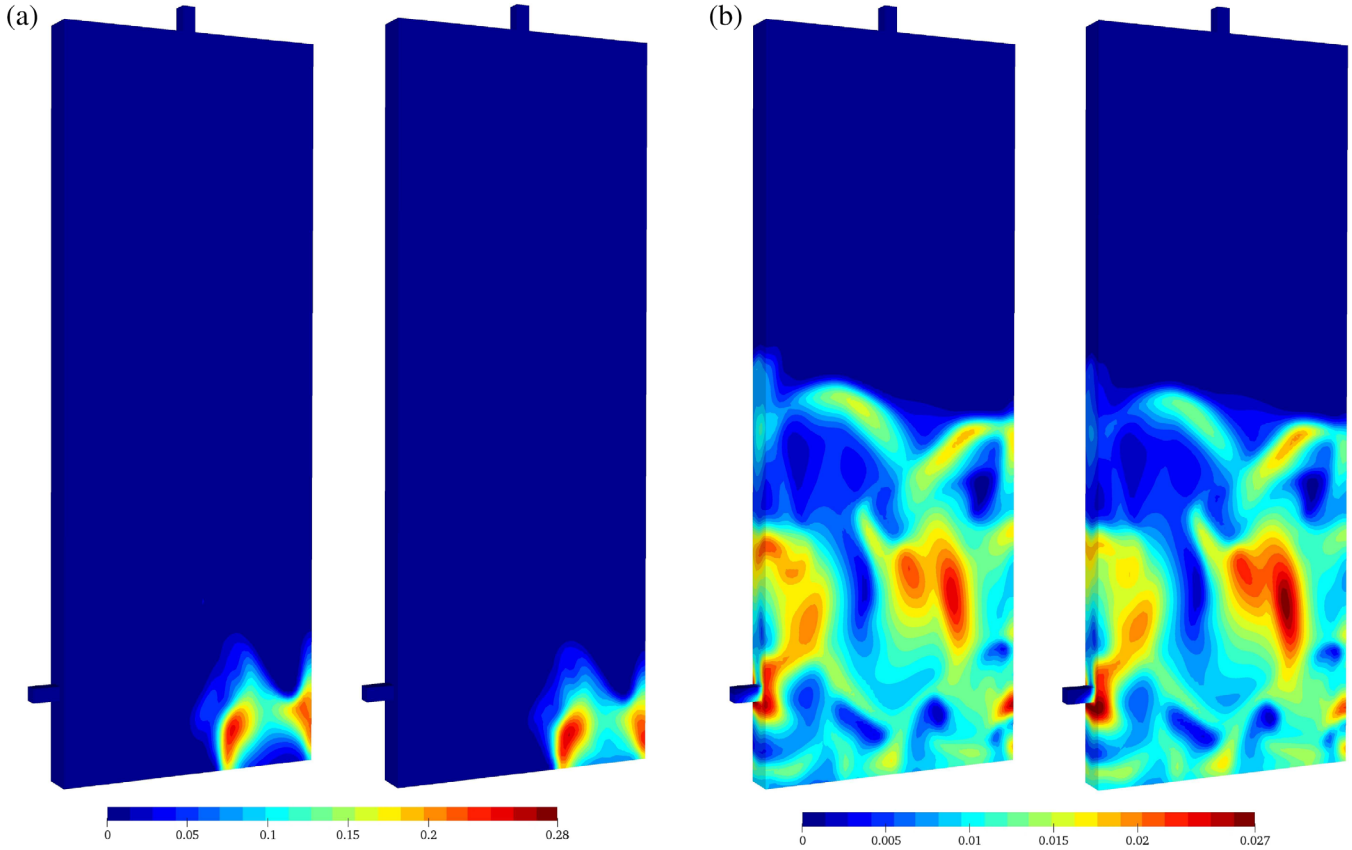

FIGURE 9 Comparative instantaneous pictures between the actual full computational fluid dynamics (CFD) red-color solid specie ($\epsilon_s\gamma$) (left) and recurrence CFD (rCFD) counterparts (right), at the moments, t = 3.16 s (a) and t = 4.6 s (b). rCFD results are obtained adopting the local diffusion approach (C = 0.8) and using $N_{tr} = 10^6$ [Color figure can be viewed at wileyonlinelibrary.com]

transportation. Namely, we use the analytical solution (complete mixing) of temperature evolution in the bulk granular material[41] to describe the interacting transport of T_g from c_0 (start cell) to c_1 (end cell) during Δt_{rec}, as follows:

$$\begin{aligned} T_g^{0.5\Delta t_{rec}} &= T_{s,c_0} + (T_{g,c_0} - T_{s,c_0})e^{-0.5\Delta t_{rec}/\mathcal{T}_{c_0}}, \\ T_{g,c_1}^{\Delta t_{rec}} &= T_{s,c_1} + \left(T_g^{0.5\Delta t_{rec}} - T_{s,c_1}\right)e^{-0.5\Delta t_{rec}/\mathcal{T}_{c_1}}, \end{aligned} \tag{14}$$

where

$$\mathcal{T}_{c_0} = \frac{\epsilon_{g,c_0}\rho_g c_p^g d_s^2}{6\epsilon_{s,c_0}\kappa_g \mathrm{Nu}_{c_0}} \quad \text{and} \quad \mathcal{T}_{c_1} = \frac{\epsilon_{g,c_1}\rho_g c_p^g d_s^2}{6\epsilon_{s,c_1}\kappa_g \mathrm{Nu}_{c_1}} \tag{15}$$

are the time scales of T_g change. Here, $T_{g,c_0} = T_{g,\mathrm{inlet}} = 300\,\mathrm{K}$ for all inlet tracers. If we name the exchanging inlet temperature as $T_{g,c_1}^{\mathrm{inlet}} = T_{g,c_1}^{\Delta t_{rec}}$, the resultant T_g transported into the target cell c_1, in case of multiple hits, is given by

$$T_g = \frac{\sum_{i=1}^{\mathrm{hits}} v_{\mathrm{inlet}}^i T_{g,c_1}^{\mathrm{inlet}}}{\sum_{i=1}^{\mathrm{hits}} v_{\mathrm{inlet}}^i}, \quad \text{with} \quad i = 1,2,\ldots,\mathrm{hits}. \tag{16}$$

During this transportation, the quantity of heat transfered due to the interaction with T_s is also summed up as

$$Q_{g,c_1} = \sum_{i=1}^{\mathrm{hits}} \epsilon_g v_{tr}^i \rho_g c_p^g \left(T_{g,c_0} - T_{g,c_1}^{\Delta t_{rec}}\right). \tag{17}$$

2. Transport T_g following the shift positions of internal gas tracers, and employing the same method before. The exchanging temperature $T_{g,c_1}^{\Delta t_{rec}}$ is evaluated from Equation (14) and the resultant T_g convected into c_1 follows:

$$T_g = \frac{\sum_{i=1}^{\mathrm{hits}} v_{tr}^i T_{g,c_1}^{\Delta t_{rec}}}{\sum_{i=1}^{\mathrm{hits}} v_{tr}^i}, \quad \text{with} \quad i = 1,2,\ldots,\mathrm{hits}. \tag{18}$$

Likewise, the amount of heat transfered Q_{g,c_1} is summed up in c_1 using Equation (17).

3. Fill the holes of T_g and Q_g fields.
4. Consider (store) T_g of the start cell outlet gas tracers $T_{g,c}^{\mathrm{outlet}}$, which leave the domain during Δt_{rec}.

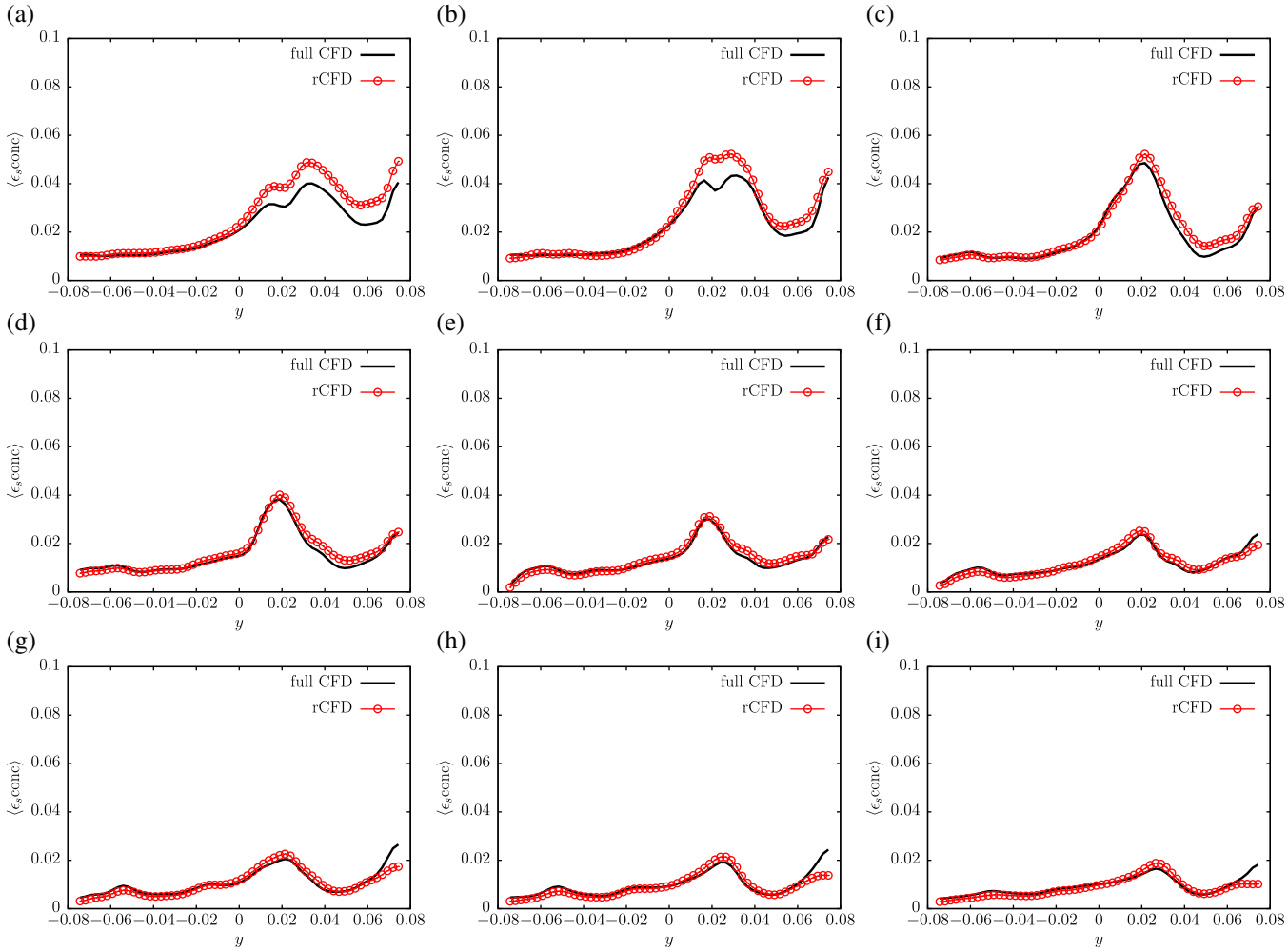

FIGURE 10 The corresponding recurrence computational fluid dynamics resultant mean profiles, extracted at the mid-width (x = 0) and different heights (a) z = 0.01, (b) z = 0.02, (c) z = 0.03, (d) z = 0.04, (e) z = 0.05, (f) z = 0.06, (g) z = 0.07, (h) z = 0.08, and (i) z = 0.09, inside the bed [Color figure can be viewed at wileyonlinelibrary.com]

5. One step correcting T_g controlled by the physical global balance between the coming-in, accumulated, exchanged and going-out gas enthalpy through the total domain, that is,

$$(mh_{\text{g}})^{t+\Delta t_{\text{rec}}} = (mh_{\text{g}})^{t} + \left(\dot{m}_{\text{in}} h_{\text{g}}^{\text{in}} - \dot{m}_{\text{out}} h_{\text{g}}^{\text{out}}\right)\Delta t_{\text{rec}} - Q_{\text{g}}, \tag{19}$$

which can be written as

$$\sum_{i=1}^{\text{cells}} \left(\epsilon_{\text{g}}^{i} T_{\text{g},c_i} V_{\text{cell}}\right)^{t+\Delta t_{\text{rec}}} = \sum_{i=1}^{\text{inlet}} v_{\text{inlet}}^{i} T_{\text{g},c_i}^{\text{inlet}} - \sum_{i=1}^{\text{outlet}} v_{\text{outlet}}^{i} T_{\text{g},c_i}^{\text{outlet}} + \sum_{i=1}^{\text{cells}} \left(\epsilon_{\text{g}}^{i} T_{\text{g},c_i} V_{\text{cell}}\right)^{t} - \frac{\sum_{i=1}^{\text{cells}} Q_{\text{g},c_i}}{\left(\rho_{\text{g}} c_{\text{p}}^{\text{g}}\right)}, \tag{20}$$

Similar to Step (5) in Section 2.2, the swapped/shifted portion of temperatures reads,

$$\Delta T_{\text{g}} = f \frac{T_{\text{g},c_i} - T_{\text{g},c_{i+1}}}{2}, \tag{21}$$

where f is dynamically decided, similar to Section 3.1.1.

6. One-step physical diffusion modeling that compensates the heat transfered by conduction in the gas phase as

$$q_{\text{g},c_i} = \left(D_{\text{g},c_i} + D_{\text{g},c_i}^{t}\right)\nabla^2 T_{\text{g},c_i}, \tag{22}$$

where $D_{\text{g},c_i} = \kappa_{\text{g}} / \left(\rho_{\text{g}} c_{\text{p}}^{\text{g}}\right)$ and $D_{\text{g},c_i}^{t} = C_{\text{g}} \Delta k_{\text{g}}^{1/2} / \text{Pr}_t$. Here, D_{g,c_i} is the molecular thermal diffusivity and D_{g,c_i}^{t} is the mixing length turbulent diffusion which is computed on the base of the turbulent kinetic energy of gas tracers k_{g} with an empirical constant C_{g} = 0.2. Pr_t = 0.4 is the turbulent Prandtl number.

Afterward, we iterate one-pass over the solid phase, transporting T_s following the solid tracers and adding the quantities of Q_g, as follows:

1. Transport T_s following the shift positions of internal solid tracers. The exchanging temperature will be

$$T_{s,c_1}^{\Delta t_{rec}} = T_{s,c_0} + \frac{Q_{g,c_1}}{\epsilon_s V_{cell} \rho_s c_p^s}, \tag{23}$$

and the resultant T_s convected into c_1 is given by

$$T_s = \frac{\sum_{i=1}^{hits} v_{tr}^i T_{s,c_1}^{\Delta t_{rec}}}{\sum_{i=1}^{hits} v_{tr}^i}, \text{with } i = 1, 2, \ldots, \text{hits}. \tag{24}$$

2. Fill the holes of T_s.
3. Consider $T_{s,c}^{outlet}$ for the solid outlet tracers that leave the domain during Δt_{rec}, and which are very rare so we can neglect them.
4. One step correcting T_s controlled by the physical global balance between the accumulated and exchanged solid enthalpy through the total domain, that is,

$$(mh_s)^{t+\Delta t_{rec}} = (mh_s)^t + Q_g, \tag{25}$$

which can be written as

$$\sum_{i=1}^{cells} \left(\epsilon_s^i T_{s,c_i} V_{cell}\right)^{t+\Delta t_{rec}} = \sum_{i=1}^{cells} \left(\epsilon_s^i T_{s,c_i} V_{cell}\right)^t + \frac{\sum_{i=1}^{cells} Q_{g,c_i}}{\rho_s c_p^s}. \tag{26}$$

Identically to the gas phase, the specific portion

$$\Delta T_s = f \frac{T_{s,c_i} - T_{s,c_{i+1}}}{2} \tag{27}$$

is swapped in or out toward T_s cells and f is dynamically decided.

5. One-step physical diffusion modeling that compensates the heat transfered by conduction in the solid phase as

$$q_{s,c_i} = \left(D_{s,c_i} + D_{s,c_i}^t\right) \nabla^2 T_{s,c_i}, \tag{28}$$

where $D_{s,c_i} = \kappa_s / \left(\rho_s c_p^s\right)$ is the molecular thermal diffusivity and similarly $D_{s,c_i}^t = C_s \Delta k_s^{1/2} / \mathrm{Pr}_t$ is the mixing length turbulent diffusion computed upon k_s with an empirical constant $C_s = \{0.2, 0.4\}$.

Applying that algorithm, the outcomes have demonstrated a practical throughout modeling of heat transfer in bubbling fluidized

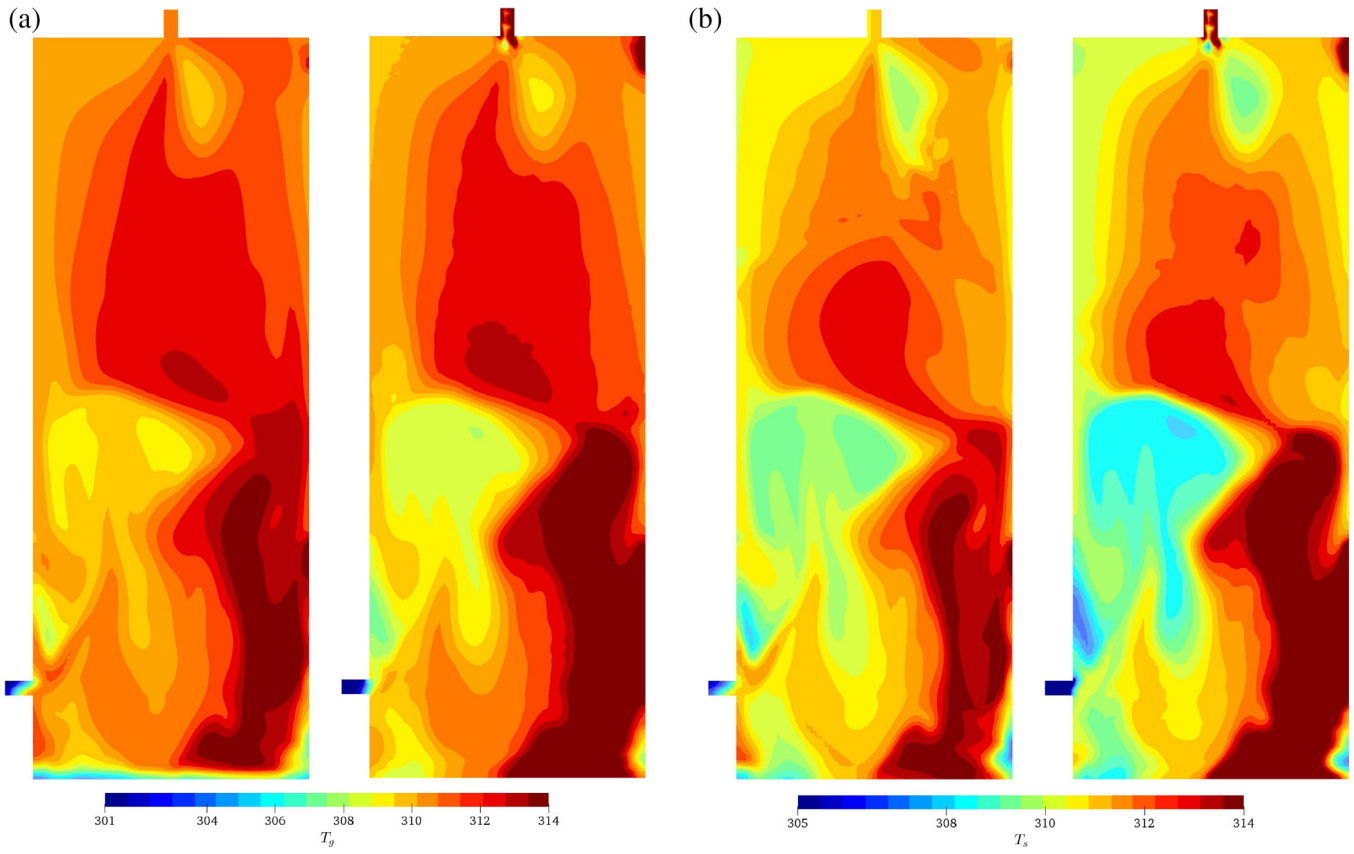

FIGURE 11 Comparative instantaneous picture of T_g (a) and T_s (b), between the actual full computational fluid dynamics (CFD) (left) and recurrence CFD (rCFD) results (right) using the local diffusion ($C_s = C_g = 0.2$), at the moment $t = 4.6$ s. The results are obtained using $N_{tr} = 5 \times 10^5$ on each phase [Color figure can be viewed at wileyonlinelibrary.com]

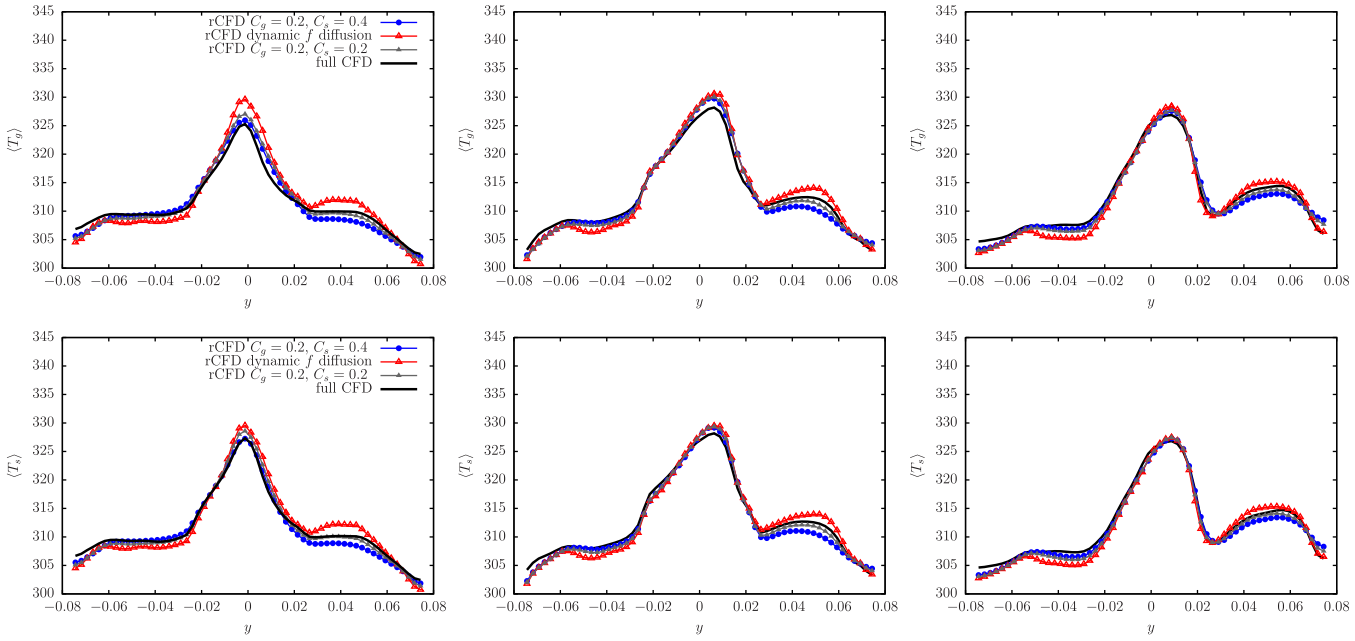

FIGURE 12 Recurrence computational fluid dynamics resultant mean profiles of $\langle T_g \rangle$ (top) and $\langle T_s \rangle$ (bottom), extracted at the mid-width $x = 0$ and different heights $z = 0.025$ (left) $z = 0.05$ (middle) and $z = 0.075$ (right) [Color figure can be viewed at wileyonlinelibrary.com]

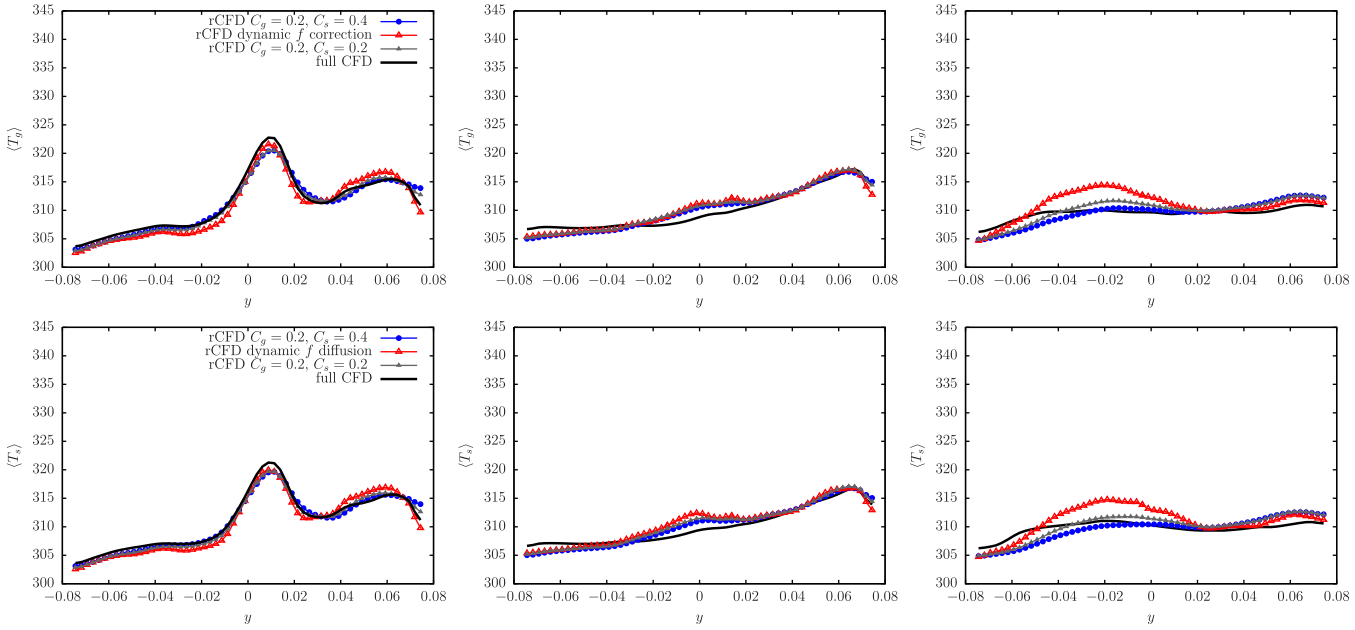

FIGURE 13 Recurrence computational fluid dynamics resultant mean profiles of $\langle T_g \rangle$ (top) and $\langle T_s \rangle$ (bottom), extracted at the mid-width $x = 0$ and different heights $z = 0.1$ (left) $z = 0.2$ (middle) and $z = 0.3$ (right) [Color figure can be viewed at wileyonlinelibrary.com]

beds by consuming a very short runtime computations (see the performance Figure 16c in Section 3.5). Analogously to species transport, an instantaneous snapshot of T_g and T_s, at $t = 4.6$ s, rendered within the mid-width plane $x = 0$, for rCFD (right) and full CFD (left) simulations is explored in Figure 11. Again, an acceptable modeling can be observed, insofar as, the exponential temporal evolution (Equations 14) and disregarding the work of expansion of the void fraction (Equations A15), are accounted as practical approximations in rCFD model. If we look at the mean temperature patterns averaged over τ^T_{rec} and showed in profiles, at ($x = 0$, y, $z = \{0.025, 0.05, 0.075\}$ m) in Figure 12 and ($x = 0$, y, $z = \{0.1, 0.2, 0.3\}$ m) in Figure 13; one can see the viable match given by rCFD modeling. Therein, the inherited enhancement of the local physical diffusion can clearly be caught, inside ($z < 0.1$ m) and outside ($z > 0.1$), the bed (see profiles at $z = 0.025$ in Figure 12 and $z = 0.3$ in Figure 13).

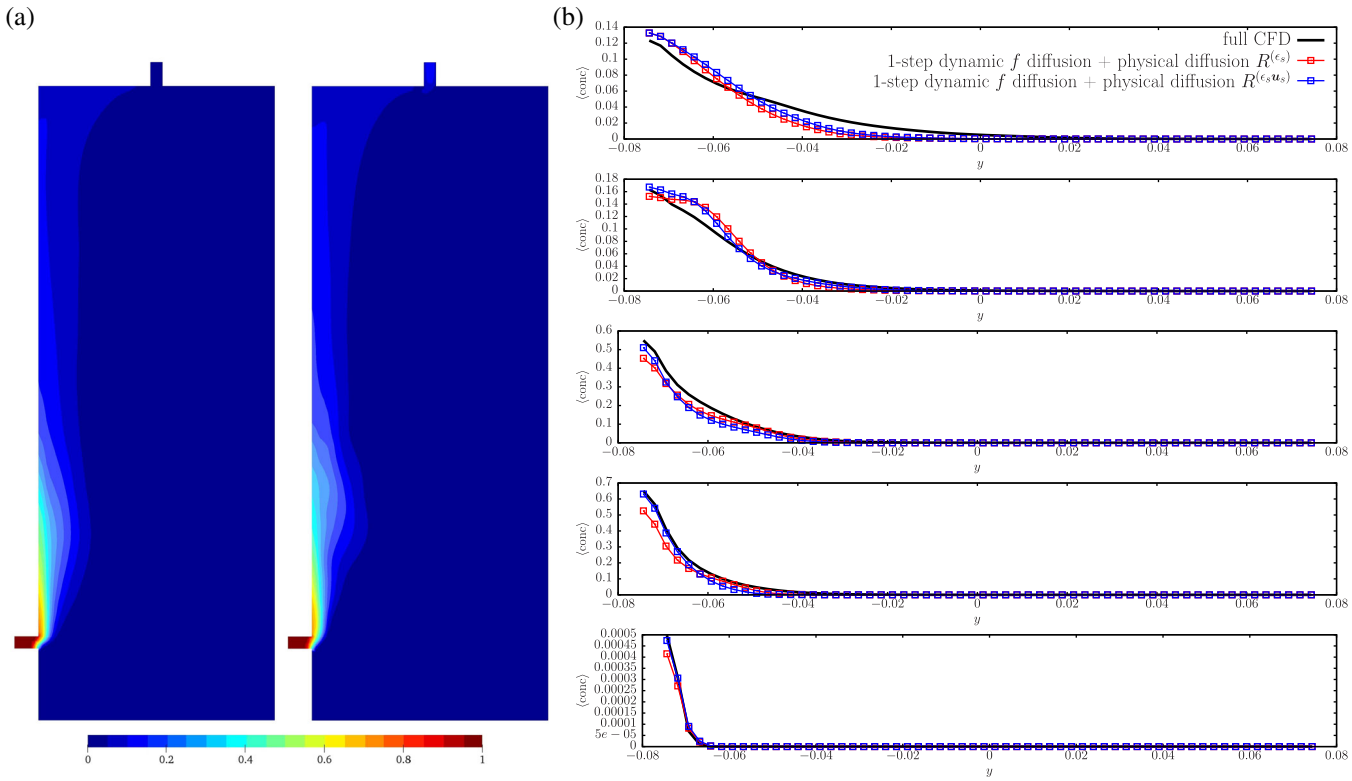

FIGURE 14 (a) Comparative mid-width (x = 0) mean pictures for the full computational fluid dynamics (CFD) species simulation (left) and recurrence CFD (rCFD) time-extrapolation results (right). The outcomes are obtained applying the local diffusion approach (C = 0.2) and following the recurrence path based on $R^{(\epsilon_s u_s)}$ matrix. (b) The corresponding resultant mean profiles, extracted at z = {0.04, 0.08, 0.1, 0.2, 0.3}, from the bottom to the top in (a), respectively. Therein, the outcomes of the recurrence path based on both $R^{(\epsilon_s)}$ and $R^{(\epsilon_s u_s)}$ matrices, are considered. All rCFD results are obtained using $N_{tr} = 10^6$ [Color figure can be viewed at wileyonlinelibrary.com]

3.4 | Time extrapolation of species transport on gas phase

The main concept of rCFD is tracing the passive scalar on stitched recurrent moments prolonged far beyond τ_{rec}, in a fast and low-cost modeling. Using the robust and randomly based approximate, depicted in Figure 1, we start from f_1 on the recurrence matrices (Figure 5) and move with arbitrary intervals and jumps, to generate in due course, a sequence of, for example, 2,000 recurrent flow frames. Sweeping over this path, the gaseous passive propagation is predicted till 22 s on the base of $\tau^{\gamma_g}_{rec}$ = 3.2s database and time step $\Delta t_{rec} = 16\Delta t$. For a comparative perspective, the concentration is traced using sequences based on $R^{(\epsilon_s)}$ and $R^{(\epsilon_s u_s)}$ recurrence matrices, and applying the favorable (one step dynamical + one step physical physical) diffusion approach in Step (5). While an accurate description of species trajectories might not be of significant interest in a long-term transfer, but its distribution on the mean picture yes. To that end, the temporal mean patterns extracted at the mid-width (y, z) plane, are drawn in Figure 14a, for $R^{(\epsilon_s u_s)}$ rCFD together with the full CFD means. One can notice the good following using the solid dynamics base which confers a better indication on the bubbles recurrence. Moreover, the similar trends, identical to Figure 8b, are unveiled in Figure 14b, to finally indicate a viable rCFD modeling of gaseous species transport using a very low computational demand (see the performance Figure 16d in Section 3.5). Digging up a consistency, the rCFD mean profiles, illustrated in Figure 14b, have shown an acceptable agreement with the full CFD counterparts bearing a foremost local deviation about 22%, in the high-γ regions. This in due time, motivates the broad applications of transport-based rCFD in predicting the long-term transport of different species, interacted chemically and thermally in fluidized bed, and propagated on both phases. This will constitute our future focus where considering a continuous thermal and chemical source is an important condition for an effective long-term transport modeling.

3.5 | Impacts and efficiency

At the crossroad between modeling accuracy and the storage needed for the empirical framework of transport-based rCFD, a Lagrangian coarse graining procedure is noteworthy.[32] Namely, by reducing the total number of tracers N_{tr}, up to which the internal seeding volume is $V_{tr} \geq V_{cell}$, the size of recurrence data frames becomes meaningfully smaller. And hence, the entire transport runtime becomes of very short extent. In order to test this impact, the reconstruction initiative of gaseous species transport is repeated on the same 400 frames using a total number of tracers, N_{tr} = 70,000, and adopting the favorable local diffusion approach. By doing so, we redo the selfsame

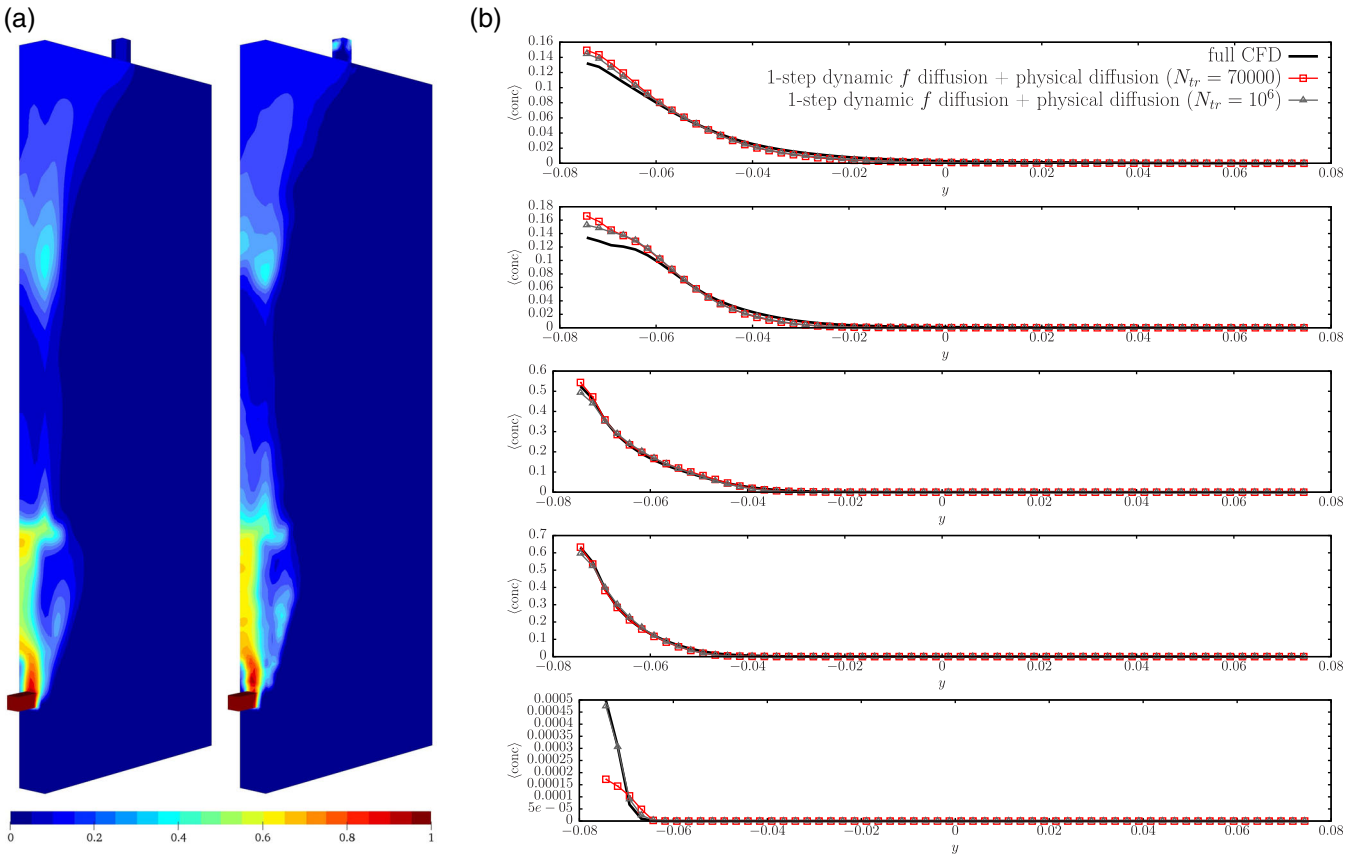

FIGURE 15 Identical representation of results, as in Figure 8, but using N_{tr} = 70,000, and applying the local diffusion approach (C = 0.2) on instant (a) and mean (b) fields. The mean analogous profiles in case of using N_{tr} = 10^6, are also shown therewith [Color figure can be viewed at wileyonlinelibrary.com]

aspects, previously outlined in Figure 8, and show them in Figure 15. From a precise look, the coarsening stratagem implies a bold transport for concentration that needs to be smoothed in-between the structures (Figure 15a). This is obviously returned to the less number of tracers that could convey more information on ϵ_g from the neighboring hit cells. In general, all procedures therein are conservative to γ mass due to the proper local diffusion applied. Nonetheless, the spatial coarse-grained transport which transfers the inertial energy following the tracers, as a large negative straining, has its influence on γ mapping. In spite of that, an attainable tracing of gaseous species transport can be obtained using N_{tr} = 70,000, and relatively gives analogous results on the mean fields (Figure 15b), spending even cheaper cost (note the performance Figure 16a,b).

Going through the rCFD performance, the computational time consumed for all current applications is graphically outlined in Figure 16. We firstly carry out an initial simulation of 3 s, needed to hit the pseudoperiodic flow, by the use of 12 CPUs and persisting over 7 hr CPU time per processor. This is followed by a short-term full CFD simulation lasting about ∼3 s, thereby the 400 flow frames of recurrence database are cached. For cases of solid species transport and heat transfer, the database is shorten to 200 flow frames with a lasting runtime ∼1.5 s. After establishing these requisites, the efficiency of the passive transportation rCFD is depicted by a comparison of one CPU runtime between rCFD and the long-term full CFD counterpart. Note that the transport-based rCFD methodology is also working, in parallel mode, on the same number of CPUs. Experiencing different approaches, as displayed in Figure 16a, the most feasible rCFD indicates a reduction of CPU time from 7 hr to 28 s, in the framework of gaseous species reconstruction and N_{tr} = 10^6 tracers. This dramatic lowering in cost implicates a speed-up ratio of 900, which is further raised to 1,575, using N_{tr} = 70,000 tracers. For the case of applying a confined molecular diffusion, the computational runtime is slightly increased to 180 s, however, it is still located in the limits of a very reliable application. Regarding the solid species reconstruction, the feasible rCFD application implies a reduction from 3.5 hr to 9 s with a 1,400 speed-up ratio, while the temperature reconstruction reduces 8 hr CPU time to 18 s with 1,600 speed-up ratio.

If we extend the gaseous species prediction much longer time, for instance, till 22 s, with a time-extrapolating rCFD, the computational efficiency is rather higher. It drastically saves an amount of 37.3 hr − 148 s = 37.29 hr (see Figure 16d) for N_{tr} = 10^6, while in the coarse-graining case the cost becomes almost negligible.

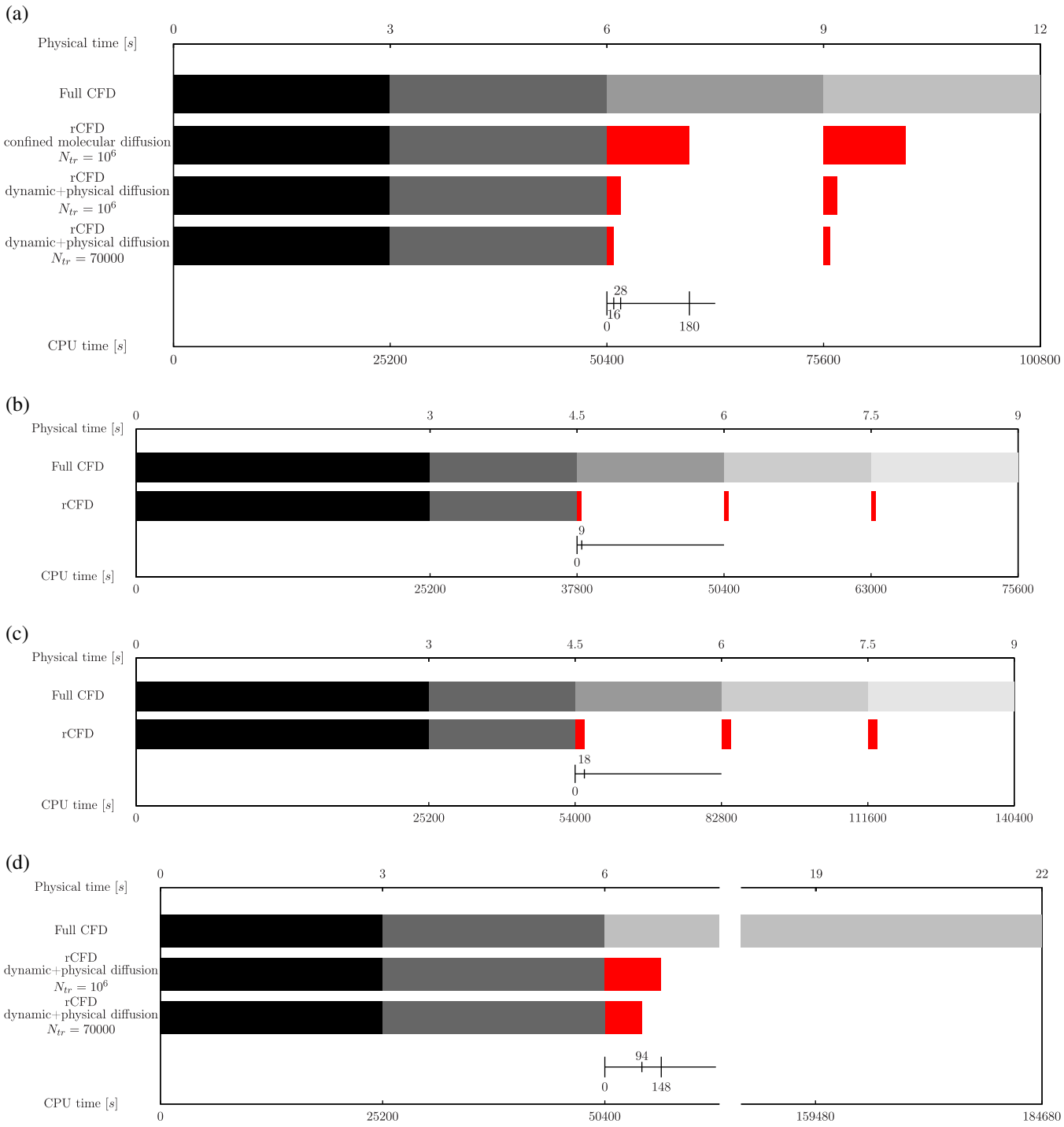

FIGURE 16 Performance of recurrence computational fluid dynamics (rCFD) modeling for the reconstruction procedure of (a) the gaseous species using different assumptions and inputs, (b) the solid species using $N_{tr} = 10^6$ and local diffusion approach, and (c) the temperature using $N_{tr} = 5 \times 10^5$ on each phase and the local diffusion approach. (d) The performance of the long-term time-extrapolation rCFD modeling for gaseous species [Color figure can be viewed at wileyonlinelibrary.com]

3.6 | Limitations

The above significant saving in computational effort comes on account of some technical and phenomenology relevant limitations. For instance, as previously outlined in Pirker et al.,[32] the pseudoperiodicity nature of the flow is an essential requirement. Even though it can clearly be remarkable on the energy containing large scales, the period of this periodicity has to be consistent and not too long. In such flows where the nonlinearity is dominant (e.g., self-organized buoyancy-driven systems), the small scales dynamics can importantly change the evolution of the total system and deliver the rCFD to sudden changes. Another difficulty can be related to the

possible fast and active interactions between chemical species. Therewith, the physical properties can be changed, and more consequences like the trigger of new solutions and heat source have to be considered. In this article, we have taken a step forward preparation to access the modeling of interacted species transportation with chemical reactions. For this regard, further constituents on reaction kinetics as production/consumption mass phase have to be tracked leading in consequence, to higher storage amount of recurrence database. This will be our primary concern in the future.

4 | CONCLUDING REMARKS

In this work, we have employed the transport-based rCFD modeling for the fast and low-cost prediction of passive species and heat transport in bubbling fluidized beds. To do so, a typical short-term full CFD simulation has been performed using the framework of TFM, to compose afterward into the backbone recurrence database. In the conceptual transport-based rCFD methodology, massless particles are used to chase the gas and solid dynamics during each recurrence period, and store the trajectories as start–end positions.[32] Herein, we have implied a physically consistent modeling for the inlet and outlet flows to be completely based on the tracers themselves. Doing so, the time-extrapolating rCFD modeling for passive transportation is applied in a more proper aspect. After the establishment of species and temperature convection, the foremost appropriate diffusion is found to be in performing one globally based diffusion step plus a kind of local physical diffusion concern. Similarly to the mixing length assumption,[40] the local physical diffusion has been approximated on the base of the turbulent kinetic energy of tracers, sampled all along the recurrence period. As a consequence, the rCFD outcomes of species and temperature reconstruction path have revealed a very reliable agreement with the full CFD (TFM) evolution by consuming a very low computational cost, and speed-up gaining up to 1,600. For large-scale simulations which commonly use coarse grids, the efficiency of rCFD can be even improved since the small scales, limiting Δt_{rec}, are not resolved but modeled in the context of filtered TFM.[19,28,29] Considering this fast and very cheap capacity, the transport-based rCFD method can constitute a strong helpful tool that allows to access and resolve many queries in the huge industrial applications.

ACKNOWLEDGEMENTS

The financial support by the Austrian Federal Ministry for Digital and Economic Affairs and the National Foundation for Research, Technology and Development is gratefully acknowledged. The authors further want to acknowledge the funding support of K1-MET GmbH, metallurgical competence center. The research programme of the K1-MET competence center is supported by COMET (Competence Center for Excellent Technologies), the Austrian programme for competence centers. COMET is funded by the Federal Ministry for Transport, Innovation and Technology, the Federal Ministry for Digital and Economic Affairs and the provinces of Upper Austria, Tyrol and Styria. Beside the public funding from COMET, this research project is partially financed by the industrial partners Primetals Technologies Austria GmbH, voestalpine Stahl Donawitz GmbH, RHI Magnesita GmbH and voestalpine Stahl GmbH.

ORCID

Firas Dabbagh https://orcid.org/0000-0001-8440-507X
Stefan Pirker https://orcid.org/0000-0003-2461-0279
Simon Schneiderbauer https://orcid.org/0000-0001-7690-9884

REFERENCES

1. Geldart D. *Gas fluidization technology*. New York: John Wiley & Sons; 1986:468.
2. Geldart D. Types of gas fluidization. *Powder Technol*. 1973;7(5):285-292.
3. Kuni D, Levenspiel O. *Fluidization Engineering*. 2nd ed. Boston, MA: Butterworth-Heinemann; 1991:491.
4. Davidson J, Harrison D. *Fluidised Particles*. Great Britain: Cambridge University Press; 1963.
5. Yang W. *Handbook of Fluidization and Fluid-Particle Systems*. Bosa Roca, United States: Taylor & Francis Inc; 2003.
6. Philippsen CG, Vilela ACF, Zen LD. Fluidized bed modeling applied to the analysis of processes: review and state of the art. *J Mater Res Technol*. 2015;4(2):208-216.
7. Beetstra R, van der Hoef MA, Kuipers JAM. Drag force of intermediate Reynolds number flow past mono- and bidisperse arrays of spheres. *AIChE J*. 2007;53(2):489-501.
8. Tang Y, Kriebitzsch S, Peters E, van der Hoef MA, JAM K. A methodology for highly accurate results of direct numerical simulations: drag force in dense gas-solid flows at intermediate Reynolds number. *Int J Multiphase Flow*. 2014;62(0):73-86.
9. Cundall PA, Strack ODL. A discrete numerical model for granular assemblies. *Gèotechnique*. 1979;29:47-65.
10. Agrawal K, Loezos PN, Syamlal M, Sundaresan S. The role of meso-scale structures in rapid gas–solid flows. *J Fluid Mech*. 2001;445:151-185.
11. Anderson TB, Jackson R. Fluid mechanical description of fluidized beds. Equations of motion. *IndEng Chem Fundamen*. 1967;6(4):527-539.
12. Tsuji Y, Kawaguchi T, Tanaka T. Discrete particle simulation of two dimensional fluidized bed. *Powder Technol*. 1993;77(1):79-87.
13. Kuipers JAM, Duin JKV, van Beckum FPH, van Swaaij WPM. A numerical model of gas-fluidized beds. *Chem Eng Sci*. 1992;47(8):1913-1924.
14. Enwald H, Peirano E, Almstedt AE. Eulerian two-phase flow theory applied to fluidization. *Int J Multiphase Flow*. 1996;22:21-66.
15. Gidaspow D. *Multiphase flow and fluidization: continuum and kinetic theory descriptions*. San Diego, CA: Academic Press, Inc.; 1994.
16. Bierwisch C, Kraft T, Riedel H, Moseler M. Three-dimensional discrete element models for the granular statics and dynamics of powders in cavity filling. *J Mech Phys Solids*. 2009;57(1):10-31.
17. Sakai M, Koshizuka S. Large-scale discrete element modeling in pneumatic conveying. *Chem Eng Sci*. 2009;64(3):533-539.
18. Radl S, Radeke C, Khinast J, Sundaresan S. Parcel-based approach for the simulation of gas-particle flows. *Proceedings of the 8th International Conference on CFD in Oil & Gas, Metallurgical and Process Industries*. Trondheim, Norway: SINTEF/NTNU; 2011:124-134.
19. Schneiderbauer S. A spatially-averaged two-fluid model for dense large-scale gas-solid flows. *AIChE J*. 2017;63(8):3544-3562.
20. Igci Y, Sundaresan S. Verification of filtered two-fluid models for gas-particle flows in risers. *AIChE J*. 2011;57(10):2691-2707.
21. Milioli CC, Milioli FE, Holloway W, Agrawal K, Sundaresan S. Filtered two-fluid models of fluidized gas-particle flows: new constitutive relations. *AIChE J*. 2013;59(9):3265-3275.

22. Ozel A, Fede P, Simonin O. Development of filtered Euler-Euler two-phase model for circulating fluidised bed: high resolution simulation, formulation and a priori analyses. *Int J Multiphase Flow*. 2013;55:43-63.
23. Parmentier JF, Simonin O, Delsart O. A functional subgrid drift velocity model for filtered drag prediction in dense fluidized bed. *AIChE J*. 2012;58(4):1084-1098.
24. Wang J, van der Hoef MA, Kuipers JAM. Coarse grid simulation of bed expansion characteristics of industrial-scale gas-solid bubbling fluidized beds. *Chem Eng Sci*. 2010;65(6):2125-2131.
25. Yang N, Wang W, Ge W, Li J. CFD simulation of concurrent-up gas-solid flow in circulating fluidized beds with structure-dependent drag coefficient. *Chem Eng J*. 2003;96(1):71-80.
26. Schneiderbauer S, Puttinger S, Pirker S. Comparative analysis of subgrid drag modifications for dense gas-particle flows in bubbling fluidized beds. *AIChE J*. 2013;59:4077-4099.
27. Schneiderbauer S, Pirker S. Filtered and heterogeneity-based subgrid modifications for gas–solid drag and solid stresses in bubbling fluidized beds. *AIChE J*. 2014;60:839-854.
28. Schneiderbauer S, Saeedipour M. Approximate deconvolution model for the simulation of turbulent gas-solid flows: an a-priori analysis. *J Phys Fluids*. 2018;30(2):023301.
29. Schneiderbauer S, Saeedipour M. Numerical simulation of turbulent gas-solid flow using an approximate deconvolution model. *Int J Multiphase Flow*. 2019;114:287-302.
30. Lichtenegger T, Pirker S. Recurrence CFD—a novel approach to simulate multiphase flows with strongly separated time scales. *Chem Eng Sci*. 2016;153:394-410.
31. Lichtenegger T, Peters EAJF, Kuipers JAM, Pirker S. A recurrence CFD study of heat transfer in a fluidized bed. *Chem Eng Sci*. 2017;172:310-322.
32. Pirker S, Lichtenegger T. Efficient time-extrapolation of single-and multiphase simulations by transport based recurrence CFD (rCFD). *Chem Eng Sci*. 2018;188:65-83.
33. Pirker S, Lichtenegger T. Process control of through-flow reactor operation by real-time recurrence CFD (rCFD) simulations—proof of concept. *Chem Eng Sci*. 2019;198:241-252.
34. Eckmann JP, Kamphorst SO, Ruelle D. Recurrence plots of dynamical systems. *Europhys Lett*. 1987;4:973-977.
35. Uddin MH, Coronella CJ. Effects of grid size on predictions of bed expansion in bubbling fluidized beds of Geldart B particles: a generalized rule for a grid-independent solution of TFM simulations. *Particuology*. 2017;34:61-69.
36. ANSYS. *Fluent theory guide*. Canonsburg, USA: ANSYS Inc.; 2018.
37. Bakshi A, Ghoniem AF, Altantzis C. Mixing dynamics in bubbling fluidized beds. *AIChE J*. 2017;63(10):4316-4328.
38. Bakshi A, Altantzis C, Glicksman LR, Ghoniem AF. Gas-flow distribution in bubbling fluidized beds: CFD-based analysis and impact of operating conditions. *Powder Technol*. 2017;316:500-511.
39. Chan TF, Golub GH, Leveque RJ. Algorithms for computing the sample variance: analysis and recommendations. *Am Stat*. 1983;37(3):242-247.
40. Pope SB. Turbulent flows. Cambridge, United Kingdom: Cambridge University Press; 2000.
41. Gutfinger C, Abuaf N. Heat transfer in fluidized beds. *Adv Heat Trans*. 1974;10:167-218.

SUPPORTING INFORMATION

Additional supporting information may be found online in the Supporting Information section at the end of this article.

How to cite this article: Dabbagh F, Pirker S, Schneiderbauer S. On the fast modeling of species transport in fluidized beds using recurrence computational fluid dynamics. *AIChE J*. 2020;66:e16931. https://doi.org/10.1002/aic.16931